The Astrophysical Journal, 974:18 (20pp), 2024 October 10 https://doi.org/10.3847/1538-4357/ad675b

The Peculiar Radio Evolution of the Tidal Disruption Event ASASSN-19bt

Collin T. Christy[1], Kate D. Alexander[1], Raffaella Margutti[2,3], Mark Wieringa[4], Yvette Cendes[5], Ryan Chornock[2], Tanmoy Laskar[6,7], Edo Berger[5], Michael Bietenholz[8], Deanne L. Coppejans[9], Fabio De Colle[10], Tarraneh Eftekhari[11,19], Thomas W.-S. Holoien[12], Tatsuya Matsumoto[13,14], James C. A. Miller-Jones[15], Enrico Ramirez-Ruiz[16], Richard Saxton[17], and Sjoert van Velzen[18]

[1] Department of Astronomy/Steward Observatory, 933 North Cherry Avenue, Room N204, Tucson, AZ 85721-0065, USA; collinchristy@arizona.edu
[2] Department of Astronomy, University of California, Berkeley, CA 94720-3411, USA
[3] Department of Physics, University of California, Berkeley, CA 94720-7300, USA
[4] CSIRO Space and Astronomy, PO Box 76, Epping, NSW 1710, Australia
[5] Center for Astrophysics | Harvard & Smithsonian, Cambridge, MA 02138, USA
[6] Department of Physics & Astronomy, University of Utah, Salt Lake City, UT 84112, USA
[7] Department of Astrophysics/IMAPP, Radboud University, PO Box 9010, 6500 GL Nijmegen, The Netherlands
[8] Department of Physics and Astronomy, York University, 4700 Keele Street, Toronto, ON M3J 1P3, Canada
[9] Department of Physics, University of Warwick, Gibbet Hill Road, Coventry, CV4 7AL, UK
[10] Instituto de Ciencias Nucleares, Universidad Nacional Autónoma de México, Apartado Postal 70-264, 04510 México, CDMX, Mexico
[11] Center for Interdisciplinary Exploration and Research in Astrophysics (CIERA) and Department of Physics and Astronomy, Northwestern University, Evanston, IL 60208, USA
[12] The Observatories of the Carnegie Institution for Science, 813 Santa Barbara Street, Pasadena, CA 91101, USA
[13] Department of Astronomy, Kyoto University, Kitashirakawa-Oiwake-cho, Sakyo-ku, Kyoto, 606-8502, Japan
[14] Hakubi Center, Kyoto University, Yoshida-honmachi, Sakyo-ku, Kyoto, 606-8501, Japan
[15] International Centre for Radio Astronomy Research, Curtin University, GPO Box U1987, Perth, WA 6845, Australia
[16] Department of Astronomy and Astrophysics, UCO/Lick Observatory, University of California, 1156 High Street, Santa Cruz, CA 95064, USA
[17] Telespazio UK for ESA, European Space Astronomy Centre, 28691 Villanueva de la Cañada, Spain
[18] Leiden Observatory, Leiden University, PO Box 9513, NL-2300 RA Leiden, The Netherlands
Received 2024 April 18; revised 2024 July 9; accepted 2024 July 23; published 2024 October 1

Abstract

We present detailed radio observations of the tidal disruption event (TDE) ASASSN-19bt/AT 2019ahk, obtained with the Australia Telescope Compact Array, the Atacama Large Millimeter/submillimeter Array, and the MeerKAT radio telescopes, spanning 40–1464 days after the onset of the optical flare. We find that ASASSN-19bt displays unusual radio evolution compared to other TDEs, as the peak brightness of its radio emission increases rapidly until 457 days post-optical discovery and then plateaus. Using a generalized approach to standard equipartition techniques, we estimate the energy and corresponding physical parameters for two possible emission geometries: a nonrelativistic spherical outflow and a relativistic outflow observed from a range of viewing angles. We find that the nonrelativistic solution implies a continuous energy rise in the outflow from $E \sim 10^{46}$ to $E \sim 10^{49}$ erg with outflow speed $\beta \approx 0.05$, while the off-axis relativistic jet solution instead suggests $E \approx 10^{52}$ erg with Lorentz factor $\Gamma \sim 10$ at late times in the maximally off-axis case. We find that neither model provides a holistic explanation for the origin and evolution of the radio emission, emphasizing the need for more complex models. ASASSN-19bt joins the population of TDEs that display unusual radio emission at late times. Conducting long-term radio observations of these TDEs, especially during the later phases, will be crucial for understanding how these types of radio emission in TDEs are produced.

Unified Astronomy Thesaurus concepts: Tidal disruption (1696); Black hole physics (159); Radio transient sources (2008); Jets (870); Accretion (14)

1. Introduction

Tidal disruption events (TDEs) arise as a natural consequence of having supermassive black holes (SMBHs) populate the centers of galaxies. These events occur when a star's orbit passes within the tidal radius of a massive black hole; for solar-type stars, this occurs outside of the event horizon for black holes with masses $M_{\rm BH} \lesssim 10^8\ M_\odot$ (Hills 1975). When a star passes close enough to be disrupted in a single flyby, roughly half of the debris escapes on hyperbolic orbits, while the remaining material circularizes to form an accretion disk around the black hole (Rees 1988). TDEs are important to study because they act as cosmic laboratories for accretion physics, outflow mechanisms, and jet formation. Radio observations in particular are used to characterize outflows in TDEs and other extragalactic transient phenomena (Alexander et al. 2020). Radio observations of transients provide key diagnostics such as calorimetry, outflow velocity, magnetic field strength, and the density of the immediate environments surrounding the transient (e.g., Chevalier 1998; Metzger et al. 2012; Margalit & Quataert 2021; Matsumoto & Piran 2023).

In recent years, many TDEs have undergone follow-up radio observations, revealing a wide range of outflow properties (see Alexander et al. 2020 for a review). A few TDEs have been observed to launch luminous, on-axis relativistic jets (e.g., Zauderer et al. 2011; Cenko et al. 2012; De Colle et al. 2012; Brown et al. 2017; Andreoni et al. 2022; Pasham et al. 2023; Yao et al. 2024) showing long-lasting luminous radio emission

[19] NHFP Einstein Fellow.

after the initial disruption of the star. More commonly, TDEs may exhibit fainter radio emission consistent with a nonrelativistic outflow from accretion-driven winds, the unbound debris expanding into the surrounding medium, and/or collision-induced outflows from the fallback stream (e.g., Strubbe & Quataert 2009; Tchekhovskoy et al. 2014; Alexander et al. 2016; Jiang et al. 2016; Krolik et al. 2016; Bonnerot & Lu 2020). However, the exact origin of the less luminous radio emission is not yet clear; any/multiple of these possibilities may be correct. It is also common for follow-up observations of TDEs to reveal no radio emission at all on timescales of days to years post-disruption, which implies the absence of an energetic outflow with emission pointing along our line of sight (van Velzen et al. 2013; Alexander et al. 2020).

Recently, as many as 40% of TDEs have been reported to show delayed ($\gtrsim$1 yr) radio emission relative to their optical discovery, suggesting that previous radio monitoring campaigns were insufficiently sensitive or ended too early (Cendes et al. 2024). An early example of such a case is the TDE ASASSN-15oi, which displayed no prompt radio emission, then a detection of a flare 6 months later, followed by a second and brighter flare years later (Horesh et al. 2021a). Another notable example is the TDE AT 2018hyz, which showed rapidly rising radio emission after 2 yr of nondetections (Cendes et al. 2022; Sfaradi et al. 2024). In a few instances, delayed low-luminosity radio emission in TDE candidates has been successfully modeled as off-axis jets (Perlman et al. 2017; Mattila et al. 2018), but the overall prevalence of jets in TDEs remains an open question hampered by inconsistent radio follow-up. Radio emission from a relativistic jet viewed off-axis may not be visible until months or years post-disruption when the jet decelerates, and in such cases, careful multifrequency modeling spanning several years may be required to discriminate between an off-axis jet and a delayed nonrelativistic outflow (Matsumoto & Piran 2023). Thus, dedicated long-term radio monitoring campaigns are necessary to fully characterize the origin(s) of radio emission in individual TDEs.

Adding to the existing set of TDE observations, we present ~4 yr of radio observations of the TDE ASASSN-19bt/AT 2019ahk. ASASSN-19bt ($z = 0.0262$) was discovered by the All-Sky Automated Survey for SuperNovae (ASAS-SN; Shappee et al. 2014; Kochanek et al. 2017) on 2019 January 29 in the galaxy 2MASX J07001137–6602251 (Holoien et al. 2019). This event marked the first TDE discovered in the Transiting Exoplanet Survey Satellite (TESS; Ricker et al. 2015) Continuous Viewing Zone, resulting in a high-cadence optical light curve. Upon this source's classification as a TDE, we quickly began our radio monitoring, with our first observation occurring near the time of peak optical emission. In their discovery paper, Holoien et al. (2019) found that the optical/UV emission of ASASSN-19bt indicated a luminosity, temperature, radius, and spectroscopic evolution similar to those of previously studied optical TDEs. However, its X-ray properties are unusual: its X-ray luminosity is among the lowest observed for any optically selected TDE, and Holoien et al. (2019) report an X-ray photon index of $\Gamma = 1.47^{+0.3}_{-0.3}$ at the time of peak optical light and $\Gamma = 2.34^{+0.8}_{-0.6}$ after optical peak, both harder than those of many optically selected TDEs (Guolo et al. 2024). Radio observations may illuminate the nature of this emission by constraining the disruption geometry and the characteristics of any resulting outflows.

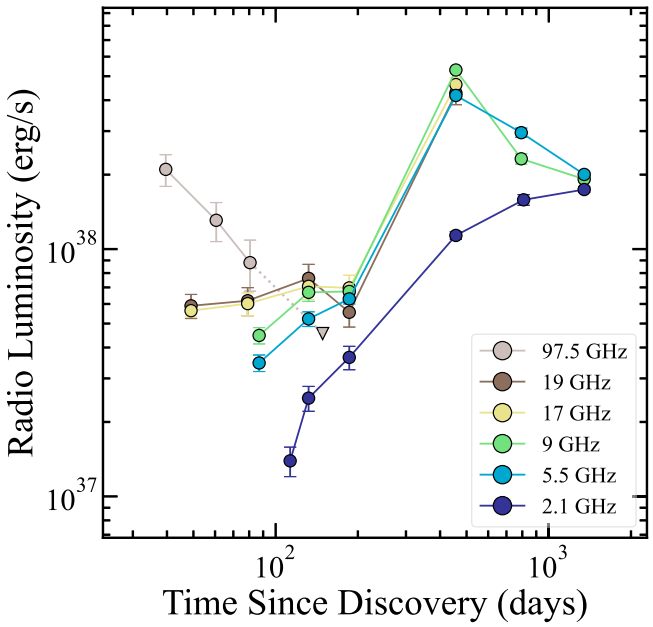

Figure 1. Radio and millimeter light curves of ASASSN-19bt, including an upper limit (3σ) from the last ALMA observation at 97.5 GHz. Our earliest radio detections occurred ~2 days before peak optical light, constraining the outflow launch time to before this date. The source brightens significantly in all observed ATCA frequencies (2.1–19 GHz) ~1 yr after the optical discovery.

In this work, we present the radio evolution of ASASSN-19bt and consider two possible models: an off-axis relativistic jet or a spherical nonrelativistic outflow. We find that the emission cannot be fully described by either of these simple limiting cases. In Section 2, we outline our observations and data reduction methods. In Section 3, we describe our modeling framework for the radio emission. In Section 4, we infer the physical properties of the outflow and the circumnuclear density for both models. In Section 5, we examine the characteristics of the outflow and discuss ASASSN-19bt in the context of other TDEs. In Section 6, we summarize our findings and present our conclusions.

2. Observations

We obtained radio, millimeter, and X-ray observations of ASASSN-19bt as described below. In addition, we also use archival X-ray and radio data and data first published in Holoien et al. (2019). We define δt as the time between our observation and 2019 January 21.6 (MJD = 58504.6), the date when the TESS light curve indicates that the transient began to brighten (Holoien et al. 2019). Additionally, we follow Holoien et al. (2019) and define the time of the optical light-curve peak as $\delta t = 42.3$ (MJD = 58546.9). We assume a distance of 115.2 Mpc for ASASSN-19bt.

2.1. Radio/Millimeter

We collected radio observations of ASASSN-19bt using the Australia Telescope Compact Array (ATCA) in the 6A, 6D, 1.5B, and 750C configurations with a frequency range of 2–19 GHz under programs C3325 (PI: K. Alexander) and CX432 (Director's Time, PI: Alexander). Additionally, we included data from 2019 March 12 under program C3148 (PI: S. van Velzen). The results of these observations can be found in Table 1 and illustrated in Figure 1. To process the data, we

applied standard data reduction techniques using the package Miriad (Sault et al. 1995). For calibration, we employed ICRF J193925.0–634245 (PKS B1934–638) as the primary flux calibrator for all observations and frequencies. PKS J0700–6610 (hereafter J0700–6610) served as the secondary calibrator for all frequencies. For the 2.1 GHz observations, we centered the field on J0700–6610 rather than slewing back and forth to the target. Due to its proximity to the TDE, we employed the "peeling" technique to improve the data calibration (see, e.g., Williams et al. 2019). This is a procedure for applying direction-dependent gains to a limited portion of an image to reduce the artifacts due to a nearby bright source.

The data were imaged using the Miriad tasks `mfclean`, `restor`. In observations where the target was sufficiently bright, we split the data into two subbands, each of bandwidth 1024 MHz, for imaging. Flux densities and their associated uncertainties were determined by fitting a point-source model (Gaussian with the width of the point-spread function) using the `imfit` command within Miriad.

We also obtained four Band 3 observations using the Atacama Large Millimeter/submillimeter Array (ALMA) with a mean frequency of 97.5 GHz under program 2018.1.01766.T (PI: K. Alexander). The data were calibrated with the ALMA data pipeline version Pipeline-CASA54-P1-B using J0519–4546 as the flux calibrator and J0700–6610 as the secondary calibrator. We detected ASASSN-19bt in the first three observations, while the 2019 June 20 observation yielded an upper limit. We imaged the data using the Common Astronomy Software Applications (CASA; version 6.2.1.7) software package (CASA Team et al. 2022), and we fit the flux densities and associated uncertainties by fitting an elliptical Gaussian fixed to the size of the synthesized beam using the CASA task `imfit`.

Finally, we obtained observations with MeerKAT at 0.82 GHz (*UHF* bands) and 1.28 GHz (*L* band) under program SCI-20210212-YC-01 (PI: Y. Cendes). For these observations, we used ICRF J040820.3–654509 as the flux calibrator and PKS J0906–6829 as the secondary calibrator. We used the calibrated images obtained via the South African Radio Astronomy Observatory Science Data Processor.[20] For these observations, we also fit the flux densities and associated uncertainties by fitting an elliptical Gaussian fixed to the size of the synthesized beam using the CASA task `imfit`.

We note that the uncertainties derived from our fitting procedure are statistical errors only. When modeling, we include an additional uncertainty of 5% of the source flux density to account for the known absolute flux density scale calibration accuracy of ATCA, ALMA, and MeerKAT. We include both sets of errors in Table 1.

2.2. Archival Radio Observations

The host galaxy of ASASSN-19bt was previously detected by ATCA serendipitously due to its proximity to J0700–6610 in observations taken at 2.1 GHz in 2015 December and 2016 August under the programs C1473 (PI: S. Ryder) and C3101 (PI: A. Edge), respectively. We reduced and imaged these data using the same procedure outlined above for our ATCA observations. The resulting archival flux densities are shown in Table 1. We detected ASASSN-bt's host galaxy in both observations. A pre-disruption radio detection implies that some of the radio emission we observe is due to background emission from the host galaxy and not associated with the TDE. If the host galaxy emission component is constant in time, then the archival radio observations and the nondetection from ALMA in 2019 imply that the host spectral energy distribution (SED) at radio frequencies follows a power law $F_\nu \propto \nu^{-0.7}$ or steeper. For our modeling, we follow the same procedure outlined in Alexander et al. (2016) and assume that the host component of the radio emission follows a single power law with $F_\nu \approx (439\,\mu\mathrm{Jy})(\nu/2.1\,\mathrm{GHz})^{-1}$, where 439 μJy is the weighted average of the two archival detections at 2.1 GHz. We note that modeling the host radio emission as a $\nu^{-0.7}$ power law instead does not significantly affect the results of our work.

We find that the archival detection is consistent with radio emission from ongoing star formation in the host galaxy. Extrapolating the quiescent component to 1.4 GHz, the observed radio luminosity requires the formation rate of stars more massive than 5 $M_\odot$ to be $\sim$0.22 $M_\odot\,\mathrm{yr}^{-1}$ (Condon et al. 2002). This is consistent with Holoien et al. (2019), who reported that an archival spectrum of 2MASX J07001137–6602251 was well fit by a star formation rate (SFR) of $0.17^{+0.06}_{-0.01}\,M_\odot\,\mathrm{yr}^{-1}$. We note that Holoien et al. (2019) did not include a possible active galactic nucleus (AGN) component when modeling the archival host galaxy spectrum; therefore, the inferred SFR should only be considered an upper limit.

Alternately, the pre-disruption radio detection could imply the presence of a compact AGN. The nondetection from ALMA suggests that if, prior to the TDE, the host contained a compact AGN with the flat radio spectrum typically seen in such sources, then its radio emission at all wavelengths must have been quenched at the time of disruption, and 100% of the emission observed during our monitoring campaign originated from the TDE. A steep-spectrum AGN component is allowed by our data, but in this case the host emission would likely arise from a relic AGN jet at a sufficiently large physical separation from the SMBH to be unaffected by the TDE. We thus conclude that it is reasonable to assume that the host galaxy emission component is constant in time.

After subtracting the host component, we find that the resulting transient component exhibits the spectral shape of a self-absorbed synchrotron spectrum in all epochs (see Figure 3). The remainder of our analysis will focus on modeling and interpreting the transient component of the radio emission. For completeness, we also model the observed emission as a single component and present our results in the Appendix; we note that these results do not alter the basic conclusions of our analysis.

2.3. X-Rays: Chandra X-Ray Observatory

We obtained two epochs of deep X-ray observations of ASASSN-19bt with the Chandra X-ray Observatory (CXO) on 2019 April 17 and 2019 June 9 (ObsIDs 22182 and 22183, PI: K. Alexander; exposure time of 9.98 ks for each ObsID), which is $\delta t = 85$ days and $\delta t = 138$ days after the optical discovery of the TDE. The data were reduced with the `CIAO` software package (v4.15) applying standard ACIS data filtering. An X-ray source is blindly detected with `wavdetect` with high statistical confidence $>4\sigma$ (Gaussian equivalent) at coordinates consistent with he optical and radio location of the TDE in each of the two CXO observations. The net 0.5–8 keV count rates are $(8.7 \pm 3.0) \times 10^{-4}$ counts s^{-1} and $(10.8 \pm 3.3) \times$

[20] https://skaafrica.atlassian.net/wiki/spaces/ESDKB/pages/338723406/

Table 1
Radio Observations of ASASSN-19bt

Date (UTC)	Telescope	Array Configuration	δt (days)	ν (GHz)	F_ν (μJy) ± Statistical Error ± Systematic Error
2015-12-07	ATCA	1.5A	−1142	2.1	464 ± 70 ± 23
2016-08-19	ATCA	6C	−886	2.1	400 ± 86 ± 20
2019-03-03	ALMA	C43-1	40	97.5	143 ± 21 ± 7
2019-03-12	ATCA	6A	49	16.7	220 ± 13 ± 11
2019-03-12	ATCA	6A	49	21.2	206 ± 23 ± 10
2019-03-24	ALMA	C43-2	61	97.5	89 ± 16 ± 4
2019-04-11	ATCA	750C	79	17.0	235 ± 25 ± 11
2019-04-11	ATCA	750C	79	19.0	216 ± 28 ± 10
2019-04-13	ALMA	C43-3	81	97.5	60 ± 14 ± 3
2019-04-19	ATCA	750C	87	5.5	418 ± 32 ± 20
2019-04-19	ATCA	750C	87	9.0	330 ± 25 ± 16
2019-05-15	ATCA	1.5B	113	2.1	440 ± 60 ± 22
2019-06-03	ATCA	6A	132	2.1	789 ± 91 ± 39
2019-06-03	ATCA	6A	132	5.5	630 ± 43 ± 31
2019-06-03	ATCA	6A	132	9.0	493 ± 40 ± 24
2019-06-03	ATCA	6A	132	17.0	276 ± 32 ± 13
2019-06-03	ATCA	6A	132	19.0	266 ± 37 ± 13
2019-06-20	ALMA	C43-9/10	149	97.5	<31
2019-07-27	ATCA	750C	186	2.1	1153 ± 125 ± 57
2019-07-27	ATCA	750C	186	5.5	759 ± 35 ± 37
2019-07-27	ATCA	750C	186	9.0	497 ± 25 ± 24
2019-07-27	ATCA	750C	186	17.0	272 ± 34 ± 13
2019-07-27	ATCA	750C	186	19.0	194 ± 25 ± 9
2020-04-23	ATCA	6A	457	2.1	3589 ± 127 ± 179
2020-04-23	ATCA	6A	457	5.0	5044 ± 91 ± 252
2020-04-23	ATCA	6A	457	6.0	4833 ± 40 ± 241
2020-04-23	ATCA	6A	457	8.5	3907 ± 38 ± 195
2020-04-23	ATCA	6A	457	9.5	3453 ± 40 ± 172
2020-04-23	ATCA	6A	457	17.0	1806 ± 115 ± 90
2020-04-23	ATCA	6A	457	19.0	1494 ± 154 ± 74
2021-03-25	ATCA	6D	793	5.0	3568 ± 154 ± 178
2021-03-25	ATCA	6D	793	6.0	3078 ± 74 ± 153
2021-03-25	ATCA	6D	793	8.5	1709 ± 83 ± 85
2021-03-25	ATCA	6D	793	9.5	1265 ± 94 ± 63
2021-04-10	ATCA	6D	809	2.1	5000 ± 250 ± 250
2021-04-19	MeerKAT	⋯	818	1.3	4400 ± 140 ± 220
2022-09-30	ATCA	6D	1347	1.6	5503 ± 140 ± 275
2022-09-30	ATCA	6D	1347	2.6	4015 ± 89 ± 200
2022-09-30	ATCA	6D	1347	5.0	2418 ± 54 ± 120
2022-09-30	ATCA	6D	1347	6.0	2087 ± 35 ± 104
2022-09-30	ATCA	6D	1347	8.5	1414 ± 37 ± 70
2022-09-30	ATCA	6D	1347	9.5	1299 ± 40 ± 64
2023-01-25	MeerKAT	⋯	1464	0.8	6764 ± 54 ± 338
2023-01-25	MeerKAT	⋯	1464	1.3	6145 ± 39 ± 307

Note. We report the uncertainties as 1σ statistical errors with an additional 5% systematic error term to account for uncertainties in the absolute flux density scale calibration. Nondetections are reported as 3σ upper limits. All values of δt are relative to 2019 January 21.6 (Holoien et al. 2019).

10^{-4} counts s^{-1}, respectively. We find no statistical evidence for temporal variability of the source in the CXO data set.

For each observation, we extracted a spectrum with `specextract` using a 1.″5 source region and a source-free background region. Due to the low number statistics, we cannot statistically constrain the spectral shape, and both thermal and nonthermal models are statistically acceptable. Adopting an absorbed simple power-law model (`tbabs*ztbabs*pow` within `Xspec`), we find best-fitting photon index values in the range $\Gamma = 1.6-1.7$ and no evidence for intrinsic absorption. The Galactic neutral hydrogen column density in the direction of ASASSN-19bt is $N_{\rm H,MW} = 7.1 \times 10^{20}$ cm^{-2} (Kalberla et al. 2005). We find no statistical evidence for spectral evolution. A joint fit of the two CXO epochs leads to the following best-fitting parameters: $\Gamma = 1.64^{+0.57}_{-0.50}$, $N_{\rm H,int} < 3.7 \times 10^{22}$ cm^{-2}, where the uncertainties are provided at the 1σ (Gaussian equivalent) confidence level (c.l.) and the upper limit at the 3σ c.l. These spectral parameters are consistent with those

Table 2
X-Ray Luminosity (0.3–10.0 keV) of ASASSN-19bt

Instrument	Observation IDs	MJD	δt	$L_X/10^{40}$ erg s^{-1}
Swift-XRT	38456001	$54853.65^{+0.17}_{-0.03}$	−3652	$16.26^{+12.44}_{-8.37}$
Swift-XRT	38456002	$54874.51^{+0.13}_{-0.13}$	−3631	<30.49
Swift-XRT	41619001	$55538.59^{+0.01}_{-0.01}$	−2967	<85.48
Swift-XRT	83377001	$56830.70^{+0.01}_{-0.01}$	−1675	<262.6
Swift-XRT	83377002	$58181.14^{+1.01}_{-0.01}$	−324	<80.28
Swift-XRT	11115001-11	$58535.23^{+9.40}_{-20.55}$	30	$4.62^{+1.91}_{-1.58}$
XMM-Newton[a]	0831791001	58543.2	38	$4.48^{+0.77}_{-0.78}$
Swift-XRT	11115012-14	$58561.71^{+0.27}_{-0.27}$	56	<9.45
Swift-XRT	11115015-22	$58581.48^{+18.86}_{-9.50}$	76	<6.07
XMM-Newton[a]	0831791101	58589.0	84	$1.24^{+0.40}_{-0.38}$
CXO-ACIS-S	22182	58591.07	85	$2.01^{+0.98}_{-0.56}$
Swift-XRT	11115024-25	$58618.17^{+3.30}_{-0.17}$	113	<25.45
CXO-ACIS-S	22183	58643.59	138	$3.18^{+0.77}_{-1.11}$
Swift-XRT	11115026-27	$58646.39^{+4.68}_{-1.37}$	141	$6.47^{+4.39}_{-3.13}$
Swift-XRT	11115028-33	$58680.73^{+10.25}_{-15.18}$	175	$4.51^{+2.54}_{-1.92}$
Swift-XRT	11115034-40	$58730.84^{+17.78}_{-12.43}$	225	$4.9^{+2.24}_{-1.79}$
Swift-XRT	11115041-45	$58802.80^{+5.11}_{-23.69}$	297	<12.12
Swift-XRT	11115046-49	$58829.49^{+0.01}_{-7.57}$	324	<16.17
Swift-XRT	11115050-54	$58840.13^{+16.66}_{-0.00}$	335	<10.6
Swift-XRT	11115055-56	$58898.48^{+7.70}_{-0.07}$	393	<26.76
Swift-XRT	11115057-63	$58940.59^{+20.75}_{-18.61}$	435	<7.48
Swift-XRT	11115064-65	$58971.52^{+4.25}_{-0.00}$	466	<17.11
Swift-XRT	11115066-67	$59177.46^{+6.18}_{-0.00}$	672	<54.95
Swift-XRT	11115069	$59193.66^{+0.01}_{-0.00}$	688	<76.33
Swift-XRT	11115072	$59206.46^{+1.34}_{-0.00}$	701	<35.08
Swift-XRT	11115073	$59219.41^{+0.00}_{-0.00}$	714	<696.02
Swift-XRT	11115075-78	$59247.70^{+0.27}_{-14.01}$	742	<27.09
Swift-XRT	96581001	$59811.58^{+0.40}_{-0.40}$	1306	<27.1
Swift-XRT	96581002	$59831.46^{+0.53}_{-0.01}$	1326	<37.73
Swift-XRT	11115079-80	$60114.40^{+3.57}_{-0.01}$	1609	<50.62

Notes. The uncertainties denote the 1σ confidence interval, while the upper limits are 3σ. We outline our reduction methods for the Chandra and Swift-XRT data in Sections 2.3 and 2.4. For discussion of the XMM-Newton data reduction, see Holoien et al. (2019).
[a] X-ray luminosity measurements are from grouped EPIC-PN, EPIC-MOS1, and EPIC-MOS2 data, and values are obtained from Holoien et al. (2019).

constrained from XMM observations in Holoien et al. (2019). The unabsorbed 0.3–10 keV fluxes and luminosities for all X-ray observations used in this work are reported in Table 2.

2.4. X-Rays: Swift-XRT

ASASSN-19bt was monitored with the X-ray Telescope (XRT; Burrows et al. 2005) on board the Neil Gehrels Swift Observatory (Gehrels et al. 2004) between 2019 January 31 and 2023 August 15 ($\delta t = 9-1666$ days). We analyzed all available Swift-XRT data using HEASoft v.6.32.1 and the corresponding calibration files. We extracted a 0.3–10 keV count-rate light curve using the online automated tools released by the Swift-XRT team (Evans et al. 2009)[21] and custom scripts (Margutti et al. 2013). A targeted search for X-ray emission from the TDE led to the detection of a weak but persistent X-ray source with an approximately constant count rate at $\delta t < 250$ days. For the count-to-flux calibration, we adopt the best-fitting spectral parameters derived from the joint fit of the two CXO epochs of Section 2.3, which leads to flux levels comparable to those inferred from the CXO and XMM. No X-ray source is detected by Swift-XRT observations acquired at $\delta t > 250$ days. However, these late-time flux limits are not deep enough to constrain the fading of the source. A persistent X-ray source with $L_X \sim$ a few 10^{40} erg s^{-1} cannot be ruled out, which makes the X-rays from ASASSN-19bt among the least luminous ever detected from an optically selected TDE (Figure 2).

We note that analyzing data serendipitously acquired by Swift-XRT years before the TDE in the same way leads to the potential identification of a source of X-ray emission in 2009, as previously reported by Holoien et al. (2019). The source is not blindly detected but has a targeted detection significance of 3σ. If real and attributed to star formation in the host galaxy, the source flux would require an SFR of $8.9^{+15.2}_{-6.4}\,M_\odot\,\mathrm{yr}^{-1}$ (Riccio et al. 2023), which is higher than the rates inferred from the archival spectra and radio detections (Section 2.2) but still consistent within a few sigma. Therefore, this marginal detection may indicate prior activity of the central SMBH or could simply be due to ongoing star formation. We further discuss the X-ray emission from ASASSN-19bt in Section 5.5.

3. Synchrotron Emission Modeling

We model the radio SEDs as synchrotron emission generated from outflowing material expanding into an external medium.

[21] https://www.swift.ac.uk/user_objects/

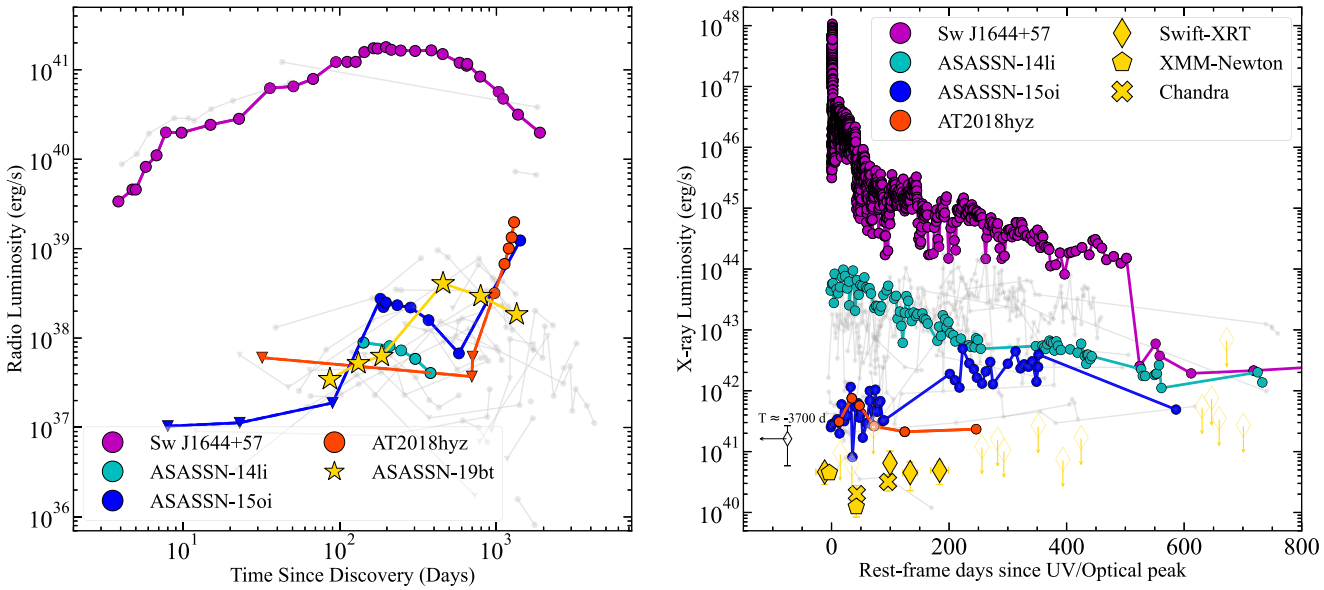

Figure 2. Left: radio luminosity of ASASSN-19bt at ≈5.5 GHz (*C* band) compared to that of a selection of previously studied TDEs with radio observations. Highlighted TDE data are for Sw J1644+57 (Zauderer et al. 2011; Eftekhari et al. 2018), ASASSN-14li (Alexander et al. 2016), ASASSN-15oi (Horesh et al. 2021a), and AT 2018hyz (Cendes et al. 2022). Gray points are data for other TDEs from the literature (Alexander et al. 2020; Cendes et al. 2024, and references therein) Right: X-ray luminosity of ASASSN-19bt (yellow symbols) compared to the sample of X-ray light curves from Guolo et al. (2024). The marginal archival X-ray detection coincident with the nucleus of ASASSN-19bt's host galaxy ∼3700 days before the TDE is shown with an open diamond. While ASASSN-19bt's radio luminosity is typical of the overall population, it has some of the faintest known X-ray emission of any TDE at both early and late times.

During this process, the blast wave generated by the outflow accelerates the electrons to a power-law distribution of energies, $N(\gamma) \propto \gamma^{-p}$ for $\gamma \geqslant \gamma_{m,0}$, immediately behind the shock; here, γ is the electron Lorentz factor, $\gamma_{m,0}$ is the minimum Lorentz factor of the shocked electrons, and p is the power-law index of the energy distribution. The shape of the synchrotron spectrum is in general a multiply broken power law, described by its break frequencies and an overall normalization factor (e.g., Granot & Sari 2002).

For ASASSN-19bt, we assume that the spectral break frequencies follow $\nu_m < \nu_a < \nu_c$, where ν_m is the typical synchrotron frequency of the minimal electron energy in the power law, ν_a is the synchrotron self-absorption frequency, and ν_c is the synchrotron cooling frequency. For the energies and high-density environments typical of most TDEs, we expect the SED peak to be located at the synchrotron self-absorption frequency and the other break frequencies to be located outside of the ATCA frequency range (e.g., Alexander et al. 2016; Cendes et al. 2021a; Goodwin et al. 2022). We therefore initially fit our data with a singly broken power law, where the peak frequency is the self-absorption frequency ν_a with $F_\nu \propto \nu^{5/2}$ below the peak and $F_\nu \propto \nu^{(1-p)/2}$ above the peak. While the peak frequency is typically associated with ν_a for nonrelativistic sources, the peak is often located at ν_m for relativistic sources at early times (Eftekhari et al. 2018; Andreoni et al. 2022). We note that instead considering the peak as ν_m in our relativistic SED modeling (Section 4.2) would not change the inferred physical parameters significantly.

We group our radio observations into seven epochs, subtract our model for the quiescent host emission (Section 2.2), and fit the remaining transient component of each SED with our synchrotron model (see the Appendix for fits to the total flux densities). Although we use the analytic SED shape from the Granot & Sari (2002) model for synchrotron emission from gamma-ray burst (GRB) afterglows for the regime where $\nu_m \ll \nu_a$, we note that we fit each SED independently, without requiring any specific dynamic evolution of the emission. The model SED is expressed as

$$F_\nu = F_{\nu,\mathrm{ext}} \left[\left(\frac{\nu}{\nu_b} \right)^{-s\beta_1} + \left(\frac{\nu}{\nu_b} \right)^{-s\beta_2} \right]^{-1/s}, \quad (1)$$

where $\beta_1 = 5/2$ and $\beta_2 = (1-p)/2$ are the spectral slopes below and above the break, $s = 1.25 - 0.18p$ describes the sharpness of the peak, and $\nu_b = \nu_a$ is the self-absorption frequency. We use the Granot & Sari (2002) analytical expression for s appropriate for an ambient density profile described by $\rho \propto r^{-2}$. This scenario most closely approximates the expected circumnuclear density profile around TDE SMBHs (Alexander et al. 2020).

We employed the Markov Chain Monte Carlo (MCMC) module `emcee` (Foreman-Mackey et al. 2013) in Python to determine the optimal model parameters, assuming a Gaussian likelihood for the measurements. We adopt uniform priors on the model parameters p, $F_{\nu,\mathrm{ext}}$, and ν_a, where $p \in [2, 4]$, $\log(F_{\nu,\mathrm{ext}}/\mathrm{mJy}) \in [-4, 2]$, and $\log(\nu_a/\mathrm{Hz}) \in [6, 11]$. In the initial modeling stage, we fit for $F_{\nu,\mathrm{ext}}$, ν_a, and p in each epoch. Our analysis revealed no significant indication of variation with time in the value of p. Therefore, we adopted a weighted average of $p = 2.80 \pm 0.02$ for the transient component ($p = 2.75 \pm 0.02$ for the total flux density fits). In our subsequent analysis, we set p to be constant at these values and only fit for $F_{\nu,\mathrm{ext}}$ and ν_a. We sampled the posterior distributions for $F_{\nu,\mathrm{ext}}$ and ν_a with 100 MCMC chains using the sampler EnsembleSampler from `emcee`. The autocorrelation lengths are ∼30–90 steps. We run each Markov chain for 5000 steps, discarding the first 1000 steps to ensure that the chains have sufficiently converged for the remaining samples. We report the best-fit transient SED parameters in Table 3, and Figure 3 shows the resulting transient SED fits (for fits to the total flux density, see Figures 10–12 in the Appendix). We attribute the

Table 3
SED Parameters from the Synchrotron Emission Model

Date (UTC)	$\langle \delta t \rangle$ (days)	ν_p (GHz)	F_p (mJy)
2019 Mar 12	49	28.56 ± 3.34	0.20 ± 0.02
2019 Apr 11/13/19	88	7.79 ± 1.22	0.25 ± 0.02
2019 Jun 3	132	4.27 ± 0.64	0.53 ± 0.06
2019 Sep 27	186	2.53 ± 0.41	0.79 ± 0.11
2020 Apr 23	457	4.03 ± 0.12	4.96 ± 0.14
2021 Mar 25/Apr 10/19	800	1.95 ± 0.09	4.46 ± 0.15
2022 Sep 30/2023 Jan 25	1377	1.06 ± 0.05	5.78 ± 0.20

Note.
We define the location of the peak frequency and flux density (ν_p, F_p) as the point on the model SED where F_ν is maximal, after accounting for curvature. We fit only the transient component of the radio flux densities.

discrepancy at higher frequencies in some epochs to phase decorrelation from the atmosphere. We do not consider this as evidence supporting an extra break, as discussed in Section 3.1.

3.1. Synchrotron Cooling

On 2019 June 20, we obtained an upper limit on the flux density at 97.5 GHz that is inconsistent with our single-break synchrotron SED model fit to the contemporaneous observations at $\lesssim$20 GHz. This discrepancy may be due to the presence of a synchrotron cooling break at a frequency of ν_c, given by (Sari et al. 1998)

$$\nu(\gamma_c) = \frac{q_e B}{2\pi m_e c}\Gamma\gamma_c^2, \tag{2}$$

where γ_c is the critical Lorentz factor required for synchrotron cooling, defined as $\gamma_c = 6\pi m_e c/\sigma_T B^2 \Gamma t$, where Γ is the bulk Lorentz factor of the shocked material and t refers to the time since the launch of the outflow in the frame of the observer. We conservatively assume that the radio outflow was launched at $\delta t = 0$ days.[22]

In Figure 4, we show the single-break SED for the data from day 132, along with a model SED that describes the single break plus synchrotron cooling. The SED model including the cooling break is given by (Granot & Sari 2002)

$$F_{\nu_c} = F_\nu \left[1 + \left(\frac{\nu}{\nu_c}\right)^{s(\beta_2-\beta_3)}\right]^{-1/s}, \tag{3}$$

where F_ν is the model described by Equation (1), $\beta_3 = -p/2$ is the spectral slope above the cooling break, and $s = 10$ describes the smoothing.[23] We fit the entire SED using Equation (3), simultaneously floating the cooling break (ν_c), self-absorption break (ν_a), and $F_{\nu,\rm ext}$. Our best-fit synchrotron cooling model suggests that $\nu_c \approx 19$ GHz. Given the expected circumnuclear density profile, the cooling break should evolve in time to higher frequencies (Granot & Sari 2002; Eftekhari et al. 2018); therefore, we attribute the poor model SED match to the higher frequencies in epochs 186–800 days as arising from phase decorrelation from the atmosphere and not from a cooling break.

Due to the B dependence of ν_c, measuring the location of the cooling break leads to an estimate of ϵ_B, the fraction of post-shock energy in magnetic fields. We outline our expressions for B explicitly in Section 4. The observed ν_c is consistent with $\epsilon_B \approx 0.2$ under the assumption that the outflow is spherical and nonrelativistic. In the off-axis jet scenario, the implied magnetic field strength B becomes a function of the observer viewing angle. We find that ϵ_B ranges from $\sim 3 \times 10^{-4}$ to $\sim$0.005 depending on the viewing angle (for exact values, see Table 5 in the Appendix).

4. Outflow Modeling

The SED fits described in Section 3 allow us to constrain the peak frequency (ν_p) and the peak flux density (F_p) in each epoch (Table 3 and Figure 5). We found that the peak flux density F_p for the transient component increases for the first five epochs then appears to plateau in the subsequent two epochs. The most dramatic brightening occurred between $\delta t \sim 186$ days and $\delta t \sim 457$ days post-discovery, with the peak flux density evolving as $t^{2.1}$ and all single-frequency radio light curves increasing by factors of $\sim$3–8. During this time range, we also find that the self-absorption frequency ν_a increases, which is unusual but not unprecedented when compared to previously seen behavior in other TDEs (e.g., Alexander et al. 2016; Eftekhari et al. 2018; Cendes et al. 2022; Goodwin et al. 2023a). We find that ν_a decays as $t^{-1.4}$ and $t^{-1.3}$ in the epochs preceding and succeeding the brightening event that occurred between days $\delta t \sim 186$ and $\delta t \sim 457$. To model the atypical evolution of the SED, we examined two scenarios: (1) the radio emission is caused by a nonrelativistic spherical outflow, or (2) the emission is due to a relativistic outflow in the form of a collimated jet viewed off-axis from the line of sight. While we initially assume that the complete radio evolution can be explained by a single outflow, we also discuss the possibility of multiple outflows in Section 5.3.

4.1. Nonrelativistic Outflow

Assuming that the observed radio emission is produced by synchrotron radiation generated in the shock between a blast wave and the ambient circumnuclear environment, we can determine the physical properties of the outflow using the procedures outlined in Barniol Duran et al. (2013). In our analysis, we associate ν_p with ν_a and assume $\nu_m < \nu_a$. Following Barniol Duran et al. (2013), we define the emitting area $f_A \equiv A/(\pi R^2/\Gamma^2)$ and the emitting volume $f_V \equiv V/(\pi R^3/\Gamma^4)$ and take $\Gamma = 1$ for an assumed nonrelativistic outflow. To compare to previously studied TDEs from the literature (e.g., Alexander et al. 2016; Cendes et al. 2021a, 2022), we assume that the emitting volume of the outflow is confined to a spherically symmetric shell of radius $0.1R$, implying $f_A = 1$ and $f_V = \frac{4}{3}(1 - 0.9^3) \approx 0.36$. With this framework, we can now derive the radius R and energy E using this geometry and the observed values of F_p and ν_p. With $p = 2.8$, the expressions for the radius and energy are given

[22] We note that while the radio outflow was not necessarily launched exactly at $\delta t = 0$ days, the launch date must be before the date of our first ALMA detection at $\delta t \approx 40$ days. This allowed range accounts for a very small fractional difference in time when considering the later epochs, so this assumption has minimal impact on our results.

[23] We note that this smoothing term is much steeper than the suggested value in Granot & Sari (2002), which was derived in the context of GRB afterglows. Instead, we adopt the smoothing parameter used in Cendes et al. (2021a) for the TDE AT 2019dsg, which was motivated by the observed sharpness of the break.

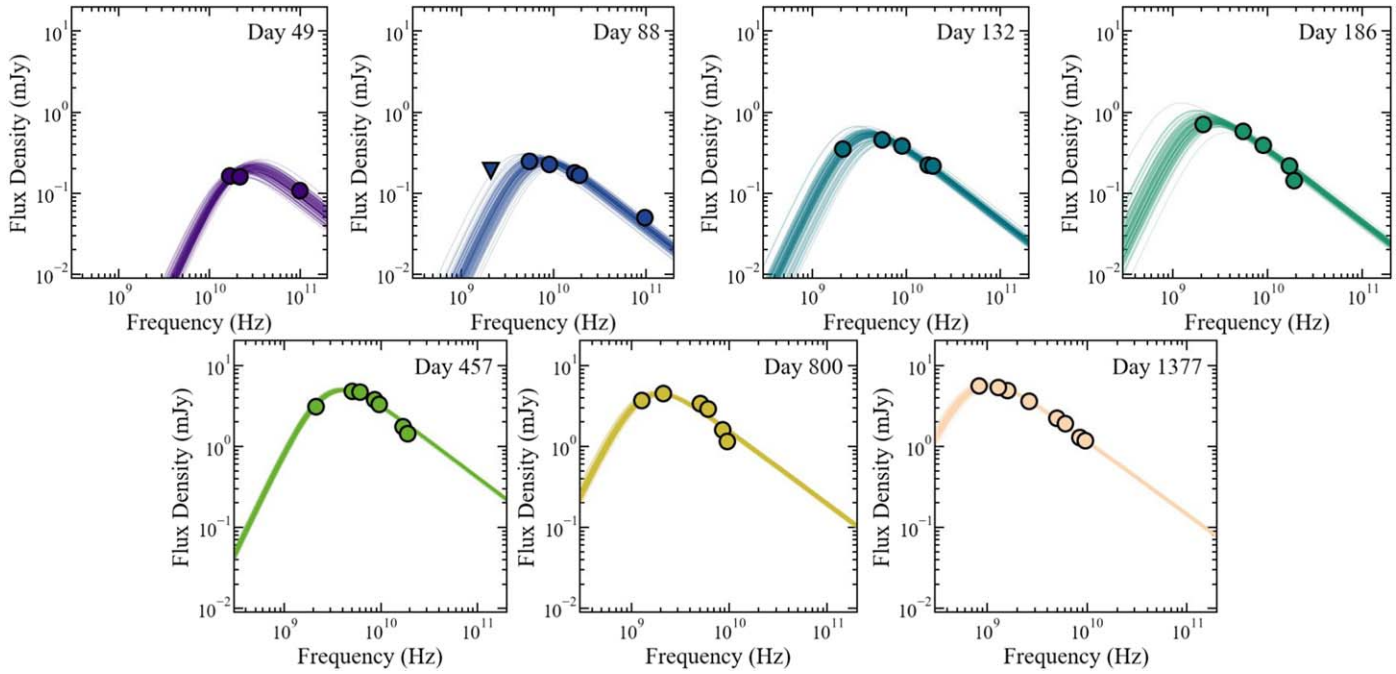

Figure 3. Radio SED fits for the combined ATCA, ALMA, and MeerKAT data obtained by subtracting the modeled quiescent emission component. The solid lines indicate a representative sample of SED fits from the MCMC modeling. The host-subtracted SEDs are characteristic of a synchrotron self-absorbed spectrum, $F_\nu \propto \nu^{(1-p)/2}$ above the peak, and consistent with $F_\nu \propto \nu^{5/2}$ below the peak. The evolution of the SED is atypical of the synchrotron emission expected from an expanding outflow as the peak frequency does not monotonically evolve to lower frequencies over time.

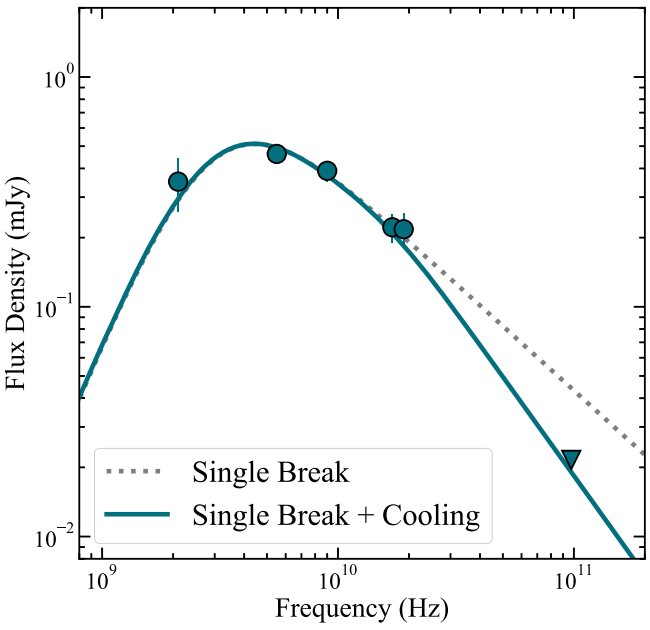

Figure 4. ATCA data along with a nondetection from ALMA at day $\langle \delta t \rangle \approx 132$ days. The dashed gray line indicates the model synchrotron self-absorbed spectrum with only one break frequency at $\nu_b \approx \nu_a$. The teal line shows the model spectrum that incorporates synchrotron cooling that finds $\nu_c \approx 19$ GHz, leading to $\epsilon_B \approx 0.2$ for a spherical Newtonian outflow and $3 \times 10^{-4} < \epsilon_B < 0.005$ for an off-axis jet depending on the viewing angle.

by (Barniol Duran et al. 2013)

$$R \approx (2.2 \times 10^{17}\mathrm{cm}) \frac{F_{p,\mathrm{mJy}}^{\frac{44}{93}} d_{L,28}^{\frac{88}{93}} \epsilon^{\frac{1}{17}} \xi^{\frac{1}{93}} 4^{\frac{1}{93}}}{\nu_{p,10} (1+z)^{\frac{137}{93}} f_A^{\frac{13}{93}} f_V^{\frac{5}{93}} \gamma_m^{\frac{4}{93}}}, \quad (4)$$

$$E \approx (2.9 \times 10^{50}\mathrm{erg}) \frac{F_{p,\mathrm{mJy}}^{\frac{112}{93}} d_{L,28}^{\frac{224}{93}} f_V^{\frac{38}{93}} \xi^{\frac{55}{93}} 4^{\frac{55}{93}} (11+6\epsilon)}{\nu_{p,10} (1+z)^{\frac{205}{93}} f_A^{\frac{19}{31}} \gamma_m^{\frac{44}{93}} (17\epsilon^{\frac{6}{17}})}, \quad (5)$$

where F_p is in units of millijansky, ν_p in units of 10 GHz, and the luminosity distance d_L in units of 10^{28} cm. In our analysis, we set the minimum Lorentz factor $\gamma_m = 2$ and incorporate additional factors of 4 as specified in Barniol Duran et al. (2013) for the Newtonian limit. We parameterize deviations from equipartition by defining $\epsilon = (11/6)(\epsilon_B/\epsilon_e)$, where ϵ_e and ϵ_B are the fractions of the total energy in electrons and the magnetic field, respectively. In our analysis, we adopt the typical value of $\epsilon_e = 0.1$ (e.g., Panaitescu & Kumar 2002) and fix $\epsilon_B = 0.2$, which is motivated by the observed location of the cooling break at 132 days (Section 3.1). We assume that the kinetic energy is dominated by the protons in the outflow; we thus incorporate the extra energy carried by the hot protons using the correction factor $\xi = 1 + \epsilon_e^{-1}$ to the total energy (Barniol Duran et al. 2013).

With the computed values of R, we can also solve for the magnetic field strength B, the Lorentz factor γ_e of the electrons that radiate at ν_p, and the total number of electrons in the observed region N_e (see Equations (14)–(16) in Barniol Duran et al. 2013). The inferred values of N_e and R allow us to estimate the density of electrons in the ambient medium at radius R as $n_{\mathrm{ext}} = n_e/4$, where $n_e = N_e/V$ is the number density of the electrons in the outflow and the factor of $1/4$ accounts for the shock jump conditions. Here, V is the emitting volume as defined above: a spherical shell with a thickness of $0.1R$ just behind the blast wave. The results of our analysis are shown in Table 4.

In Figure 6, we show the temporal evolution of the emitting region size R and the corresponding minimum equipartition energy E. The size of the synchrotron emitting region increases

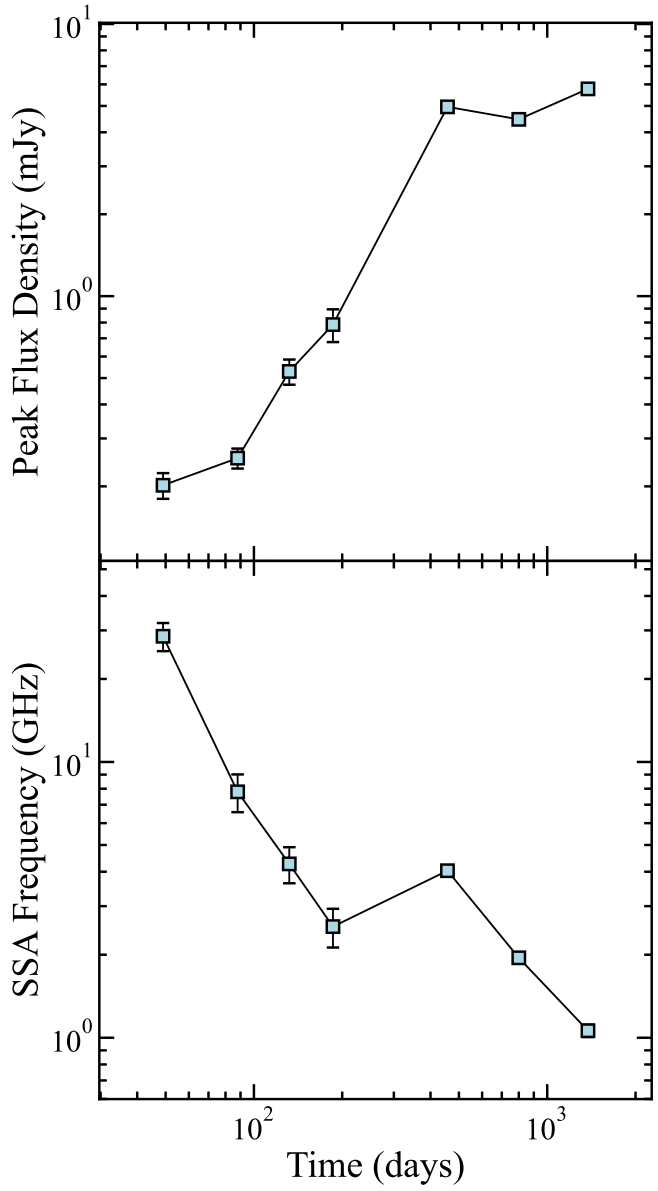

Figure 5. Top: the evolution of the observed peak flux density derived from the SED modeling. The peak flux density increases with time as a power law at early times, then remains approximately constant. Bottom: the evolution of the synchrotron self-absorption (SSA) frequency (ν_a) derived from the SED modeling. ν_a decays with time as a power law at early and late times; however, the late-time evolution is disjoint from the earlier epochs.

monotonically with time, as one would expect for an expanding outflow. Including all epochs, the radius expands at a rate of $R \propto t^{1.3}$; however, the four observations in 2019 ($\delta t = 49-186$) follow a much steeper trend of $R \propto t^{2.3}$, and from 2020 onward ($\delta t = 457-1377$), the radius increases as $R \propto t^{1.3}$. The minimum energy of this region also shows a positive trend in time, increasing more than 3 orders of magnitude as $E \propto t^{2.2}$ over the full 4 yr of observation. The inferred specific momentum ($\Gamma\beta$) also goes up with time for some portion of the light curve. We construct a radial profile for the magnetic field strength (see Figure 6). We find that the magnetic field decays with increasing radius as $B(r) \propto r^{-0.8}$ at early times and as $B(r) \propto r^{-1}$ at late times. For discussion of the density profile, see Section 5.2.

4.2. Relativistic Jet from an Arbitrary Viewing Angle

Given the nearby ($z = 0.0262$) location of this TDE, the radio luminosity, evolution timescale, and lack of detected γ-ray emission suggest that this outflow is not due to a relativistic jet pointed toward the observer, or on-axis. However, the appearance of a relativistic or collimated outflow can change due to the viewing angle. If a relativistic jet were to be launched off-axis, the emission would be suppressed at early times due to relativistic beaming away from the viewer. As the jet decelerates, the observer may begin seeing emission from inside the beaming cone.

We examined the possibility of a relativistic jet in ASASSN-19bt by employing the model outlined in Matsumoto & Piran (2023). This work generalizes Barniol Duran et al.'s (2013) analysis of an on-axis relativistic jet in energy equipartition to consider a jet observed from arbitrary viewing angles. Here, we briefly summarize this model and update the equations from Matsumoto & Piran (2023) to account for deviations from energy equipartition and the additional kinetic energy carried by hot protons, as we did in Section 4.1. Unless otherwise specified, all variables have the same definitions as in Section 4.1.

In the relativistic limit, there are two additional degrees of freedom: the jet Lorentz factor Γ and the viewing angle $\theta_{\rm obs}$ between the observer's line of sight and the source's direction of motion. The energy therefore does not have a global minimum, and we require an additional constraint on the system to solve for the physical parameters of the jet as we did above. We obtain this constraint by making an assumption about the outflow launch time, following Matsumoto & Piran (2023). As in Section 3.1, we take the launch time to be $\delta t = 0$ days.

Following the procedure outlined in Matsumoto & Piran (2023), we first solved for the radius that minimizes the total energy under a $p = 2.8$ power-law distribution of electrons. In this model, the observed location of the cooling break implies $3 \times 10^{-4} < \epsilon_B < 0.005$ depending on the viewing angle (Table 5 in the Appendix gives the precise values). This suggests that the system is not in equipartition; therefore, as in the nonrelativistic case, we incorporate additional terms to accommodate this deviation following Barniol Duran et al. (2013). For $p = 2.8$, the corresponding radius and energy are

$$R \approx (2.4 \times 10^{17}\ {\rm cm}) \frac{F_{p,{\rm mJy}}^{\frac{44}{93}} d_{L,28}^{\frac{88}{93}} \Gamma \epsilon^{\frac{1}{12}} \xi^{\frac{1}{93}}}{\nu_{p,10} (1+z)^{\frac{137}{93}} f_A^{\frac{13}{93}} f_V^{\frac{5}{93}} \gamma_m^{\frac{4}{93}} \delta_D^{\frac{13}{31}}}, \quad (6)$$

$$E \approx (6.6 \times 10^{50}\ {\rm erg}) \frac{F_{p,{\rm mJy}}^{\frac{112}{93}} d_{L,28}^{\frac{224}{93}} f_V^{\frac{38}{93}} \xi^{\frac{55}{93}} \Gamma (11 + 6\epsilon)}{\nu_{p,10} (1+z)^{\frac{205}{93}} f_A^{\frac{19}{31}} \gamma_m^{\frac{44}{93}} \delta_D^{\frac{81}{31}} (17\epsilon^{\frac{5}{12}})}. \quad (7)$$

In this case, $\gamma_m = \chi_e(\Gamma - 1)$, where $\chi_e = (p-2/p-1)\epsilon_e(m_p/m_e)$, and $\delta_D \equiv 1/\Gamma(1 - \beta\cos\theta_{\rm obs})$ is the relativistic Doppler factor for a given source velocity $\beta = \sqrt{1 - 1/\Gamma^2}$. The additional terms involving ξ and ϵ account for hot protons and deviations from equipartition with the same definitions as in Section 4.1. We solve for Γ in each epoch using the same procedure outlined Matsumoto & Piran (2023).

We initially set the jet area and volume filling factors to be $f_A = f_V = 1$. This accounts only for energy within an angle of $1/\Gamma$ from our line of sight. Material at larger angles will contribute negligibly to the observed emission due to relativistic beaming, so this provides the minimum energy required to

Table 4
Physical Parameters Derived from Our Analysis Assuming Differing Outflow Geometries

Geometry	$\langle\delta t\rangle$ (days)	log(R) (cm)	log(E) (erg)	log($E_{\rm wide}$) (erg)	log(B) (G)	log(N_e)	log($n_{\rm ext}$) (cm^{-3})	β
Spherical	49	$15.30^{+0.05}_{-0.04}$	$46.40^{+0.05}_{-0.04}$	⋯	$0.86^{+0.04}_{-0.05}$	$50.57^{+0.05}_{-0.04}$	$4.01^{+0.09}_{-0.09}$	$0.016^{+0.002}_{-0.001}$
$f_A = 1$	88	$15.91^{+0.09}_{-0.06}$	$47.08^{+0.12}_{-0.09}$	⋯	$0.29^{+0.07}_{-0.07}$	$51.26^{+0.12}_{-0.09}$	$2.85^{+0.15}_{-0.13}$	$0.036^{+0.008}_{-0.005}$
$f_V = 0.36$	132	$16.32^{+0.08}_{-0.07}$	$47.72^{+0.11}_{-0.10}$	⋯	$-0.01^{+0.06}_{-0.06}$	$51.89^{+0.11}_{-0.10}$	$2.26^{+0.14}_{-0.11}$	$0.062^{+0.011}_{-0.010}$
$\epsilon_e = 0.1$	186	$16.64^{+0.11}_{-0.08}$	$48.16^{+0.16}_{-0.11}$	⋯	$-0.26^{+0.07}_{-0.07}$	$52.34^{+0.16}_{-0.11}$	$1.77^{+0.15}_{-0.12}$	$0.090^{+0.023}_{-0.016}$
$\epsilon_B = 0.2$	457	$16.81^{+0.02}_{-0.02}$	$48.92^{+0.02}_{-0.02}$	⋯	$-0.14^{+0.02}_{-0.01}$	$53.09^{+0.02}_{-0.02}$	$2.01^{+0.03}_{-0.03}$	$0.055^{+0.002}_{-0.002}$
	800	$17.11^{+0.02}_{-0.03}$	$49.18^{+0.03}_{-0.03}$	⋯	$-0.45^{+0.02}_{-0.02}$	$53.35^{+0.03}_{-0.03}$	$1.38^{+0.05}_{-0.04}$	$0.062^{+0.003}_{-0.004}$
	1377	$17.42^{+0.03}_{-0.02}$	$49.57^{+0.04}_{-0.03}$	⋯	$-0.73^{+0.02}_{-0.03}$	$53.75^{+0.04}_{-0.03}$	$0.83^{+0.04}_{-0.05}$	$0.074^{+0.006}_{-0.004}$
Geometry	$\langle\delta t\rangle$ (days)	log(R) (cm)	log(E) (erg)	log($E_{\rm wide}$) (erg)	log(B) (G)	log(N_e)	log($n_{\rm ext}$) (cm^{-3})	Γ
Jet	49	$17.28^{+0.01}_{-0.01}$	$50.48^{+0.07}_{-0.07}$	$52.21^{+0.11}_{-0.12}$	$0.54^{+0.05}_{-0.07}$	$52.83^{+0.05}_{-0.04}$	$3.31^{+0.09}_{-0.10}$	$51.2^{+3.3}_{-3.7}$
$\theta_{\rm obs} = 1.05$	88	$17.54^{+0.01}_{-0.01}$	$50.35^{+0.09}_{-0.09}$	$51.56^{+0.22}_{-0.17}$	$-0.17^{+0.10}_{-0.09}$	$52.86^{+0.05}_{-0.06}$	$2.05^{+0.18}_{-0.14}$	$28.3^{+3.4}_{-3.7}$
$f_A = 1$	132	$17.71^{+0.01}_{-0.01}$	$50.46^{+0.07}_{-0.06}$	$51.31^{+0.22}_{-0.14}$	$-0.56^{+0.10}_{-0.08}$	$53.04^{+0.03}_{-0.04}$	$1.35^{+0.18}_{-0.12}$	$19.0^{+2.7}_{-2.1}$
$f_V = 1$	186	$17.86^{+0.01}_{-0.01}$	$50.54^{+0.08}_{-0.08}$	$51.15^{+0.23}_{-0.17}$	$-0.86^{+0.10}_{-0.10}$	$53.17^{+0.04}_{-0.05}$	$0.80^{+0.19}_{-0.15}$	$14.4^{+2.2}_{-2.2}$
$\epsilon_e = 0.1$	457	$18.25^{+0.01}_{-0.01}$	$51.78^{+0.02}_{-0.02}$	$52.72^{+0.05}_{-0.04}$	$-0.66^{+0.02}_{-0.02}$	$54.24^{+0.01}_{-0.01}$	$1.02^{+0.04}_{-0.03}$	$20.8^{+0.6}_{-0.5}$
$\epsilon_B = 0.003$	800	$18.50^{+0.01}_{-0.01}$	$51.93^{+0.02}_{-0.02}$	$52.79^{+0.07}_{-0.05}$	$-0.99^{+0.03}_{-0.03}$	$54.41^{+0.01}_{-0.01}$	$0.39^{+0.06}_{-0.04}$	$19.0^{+0.9}_{-0.7}$
	1377	$18.73^{+0.01}_{-0.01}$	$52.14^{+0.02}_{-0.03}$	$52.89^{+0.06}_{-0.07}$	$-1.30^{+0.03}_{-0.04}$	$54.65^{+0.02}_{-0.02}$	$-0.20^{+0.05}_{-0.06}$	$16.7^{+0.7}_{-0.9}$
Jet	49	$17.02^{+0.01}_{-0.01}$	$50.24^{+0.07}_{-0.07}$	$51.37^{+0.11}_{-0.12}$	$0.66^{+0.05}_{-0.07}$	$52.70^{+0.05}_{-0.04}$	$3.38^{+0.09}_{-0.10}$	$25.7^{+1.6}_{-1.9}$
$\theta_{\rm obs} = 1.57$	88	$17.27^{+0.01}_{-0.01}$	$50.12^{+0.09}_{-0.09}$	$50.72^{+0.22}_{-0.17}$	$-0.04^{+0.10}_{-0.09}$	$52.73^{+0.05}_{-0.06}$	$2.12^{+0.18}_{-0.14}$	$14.2^{+1.7}_{-1.8}$
$f_A = 1$	132	$17.44^{+0.01}_{-0.01}$	$50.23^{+0.07}_{-0.06}$	$50.48^{+0.22}_{-0.14}$	$-0.43^{+0.10}_{-0.08}$	$52.90^{+0.04}_{-0.04}$	$1.42^{+0.18}_{-0.12}$	$9.5^{+1.3}_{-1.1}$
$f_V = 1$	186	$17.59^{+0.01}_{-0.01}$	$50.30^{+0.08}_{-0.08}$	$50.31^{+0.23}_{-0.17}$	$-0.73^{+0.10}_{-0.10}$	$53.03^{+0.04}_{-0.05}$	$0.87^{+0.19}_{-0.15}$	$7.2^{+1.1}_{-1.1}$
$\epsilon_e = 0.1$	457	$17.98^{+0.01}_{-0.01}$	$51.55^{+0.02}_{-0.02}$	$51.88^{+0.05}_{-0.04}$	$-0.53^{+0.02}_{-0.02}$	$54.11^{+0.01}_{-0.01}$	$1.09^{+0.04}_{-0.03}$	$10.4^{+0.3}_{-0.3}$
$\epsilon_B = 0.005$	800	$18.23^{+0.01}_{-0.01}$	$51.69^{+0.02}_{-0.02}$	$51.95^{+0.07}_{-0.05}$	$-0.87^{+0.03}_{-0.03}$	$54.28^{+0.01}_{-0.02}$	$0.46^{+0.06}_{-0.05}$	$9.5^{+0.5}_{-0.3}$
	1377	$18.46^{+0.01}_{-0.01}$	$51.91^{+0.02}_{-0.03}$	$52.05^{+0.06}_{-0.07}$	$-1.17^{+0.03}_{-0.04}$	$54.51^{+0.02}_{-0.02}$	$-0.13^{+0.05}_{-0.06}$	$8.3^{+0.4}_{-0.4}$

Note. $\langle\delta t\rangle$ is the time since discovery in units of days; all other parameters are in cgs units.

explain our observations at each epoch. However, a jet with an evolving opening angle of $\theta_{\rm j} = 1/\Gamma$ is not physically likely; while we do eventually expect lateral spreading of the jet as it decelerates, theoretical work suggests that jet spreading is likely not yet important at the large bulk Γ values required by our observations (Duffell & Laskar 2018). We therefore also consider other possible jet geometries in which the jet opening angle remains fixed independent of Γ. We did not include any narrow jet geometries ($\theta_{\rm j} < 1/\Gamma$), as the implied jet opening angle became nonphysical due to large bulk Γs. We do investigate the effect of a wide jet geometry by accounting for additional energy outside the beamed emission region within an angle of $1/\Gamma$, which contributes negligibly to the observed emission but increases the total energy of the jet. The true collimation of TDE jets is still unknown. AGN jets are typically seen to have $\Gamma \lesssim 10$ with opening angles around $\theta_j \sim 20°$, whereas GRBs have been seen to launch highly collimated jets with $\Gamma \sim 100$ with opening angles often below 10° (Goldstein et al. 2016; Pushkarev et al. 2017; Rouco Escorial et al. 2023). Therefore, for our analysis, we impose an intermediate jet opening angle of $\theta_j = 10°$. For this fixed opening angle, we are always in the regime where $\theta_j > 1/\Gamma$ and subsequently correct for the unseen material by multiplying the equipartition energy by a factor of $4\Gamma^2(1 - \cos\theta_{\rm j})$. The other derived quantities are unaffected, as they depend only on the emission within the observable region (so we can keep $f_A = f_V = 1$ throughout).

In Figure 6, we show our derived physical parameters for six possible viewing angles: $\theta_{\rm obs} = 0.1$, 0.26, 0.52, 0.79, 1.05, and 1.57 (i.e., 6°, 15°, 30°, 45°, 60°, and 90°). We find that the solutions become extreme for small viewing angles. Solutions for the most on-axis case we tested ($\theta_{\rm obs} \approx 6°$) resulted in unphysical outflow velocities of $\Gamma > 1000$ and energies approaching 10^{54} erg. These solutions diverge to higher energies for small $\theta_{\rm obs}$ due to the large beaming effects needed to reduce the observed flux toward the observer. We find that our most reasonable solutions appear to be when we consider the relativistic outflow as a highly off-axis collimated jet (the two most off-axis cases are shown in Table 4). A jet truly spreading with $\theta_{\rm j} = 1/\Gamma$ would exhibit two periods of roughly constant energy at $\sim 2 \times 10^{50}$ erg from ∼50 to 190 days and $\sim 7 \times 10^{51}$ erg from ∼460 to 1380 days. The wide jet geometry with $\theta_{\rm j} = 10°$ instead implies that the energy decreases by a factor of ∼10 during the first 200 days, then remains constant at $E \sim 10^{52}$ erg at later times. All viewing angles yield a solution where the jet propagates at nearly light speed with $\Gamma \sim 10-20$ for the most off-axis viewing angles. We find that the jet slows as $\Gamma \propto t^{-1}$. After the radio rebrightening, we find that Γ exhibits a weaker decay where $\Gamma \propto t^{-0.2}$. We note that Γ is dependent on the inferred launch date of the jet; for a discussion of alternative launch dates, see Section 5.3.

5. Discussion

Each of the two models discussed in Section 4 provides a reasonable fit to the data, but each has some implications that are difficult to explain. Here, we present the implications of these two models and compare ASASSN-19bt to other TDEs in the literature.

Aspects of ASASSN-19bt's radio light curve resemble those of a few other known TDEs (Figure 7), many of which have

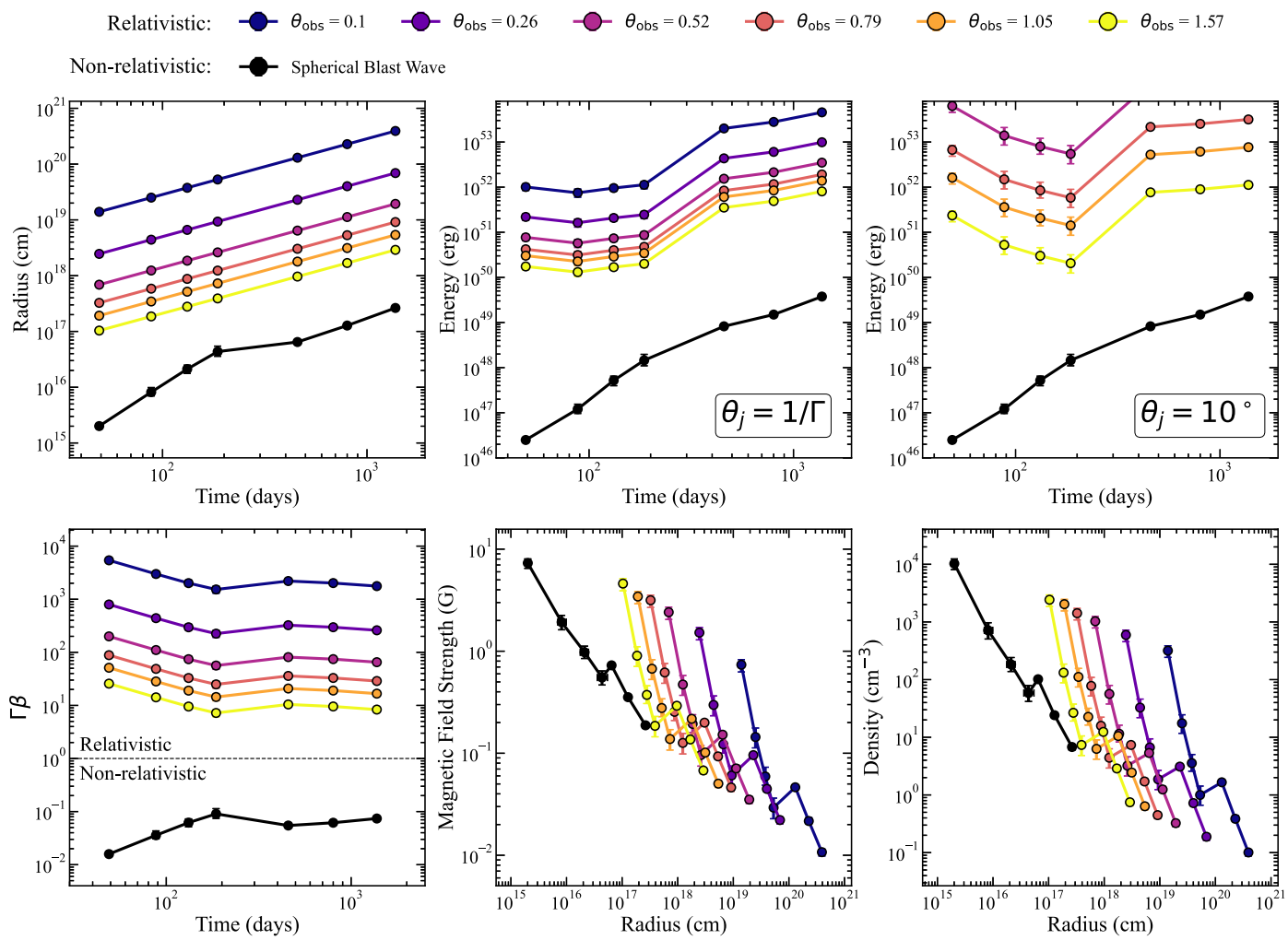

Figure 6. The temporal and radial dependencies of the physical parameters derived from our analysis of the synchrotron model fits. In each panel, we show the results for the nonrelativistic outflow model presented in Barniol Duran et al. (2013; black circles) and the relativistic solution proposed in Matsumoto & Piran (2023; indigo–yellow circles) for a set of off-axis viewing angles. We show the radius of the emitting region as a function of time (top left), the outflow kinetic energy as a function of time for a jet with $\theta_j = 1/\Gamma$ (top middle), the outflow kinetic energy as a function of time assuming a fixed jet opening angle $\theta_j = 10°$ (top right), the velocity evolution of outflow (bottom left), the radial profile of the magnetic field (bottom middle), and the radial profile of the number density of electrons in the emitting region (bottom right). The error bars on the data correspond to 1 standard deviation computed using an MCMC approach. The quantities shown here are summarized in Table 4.

displayed delayed radio brightening a few years after discovery (e.g., Horesh et al. 2021a, 2021b; Cendes et al. 2022, 2024; Goodwin et al. 2022). At early times, ASASSN-19bt's rise appears most similar to the slow one seen in AT 2019azh (Goodwin et al. 2022). AT 2019azh also exhibited a late-time flare at a similar time to ASASSN-19bt's brightening (Sfaradi et al. 2022). The origin of the radio emission in AT 2019azh was difficult to determine, with only the unbound debris stream ruled out as a possibility (Goodwin et al. 2022). The late-time evolution and observed luminosity of ASASSN-19bt are also similar to those of IGR J12580+0134 and ARP 299-B AT1, TDEs with suspected off-axis relativistic jets (Lei et al. 2016; Mattila et al. 2018). However, its radio evolution is quite different from that of two other TDEs that may harbor powerful jets: AT 2018hyz, which may have an off-axis jet and continues to brighten rapidly >1000 days post-discovery, and Sw J1644+57, which had an on-axis jet but remained much more luminous than ASASSN-19bt at every phase of its evolution (even at late times when its jet has decelerated and the observed emission should be independent of the viewing angle). We develop these comparisons further below.

5.1. Energy and Velocity

We show the outflow kinetic energy and inferred velocity of ASASSN-19bt in comparison to those of known TDEs in Figure 8. As mentioned previously, ASASSN-19bt exhibits a dramatic energy increase under the Newtonian model, increasing by 3 orders of magnitude over the period of our observations. This is by far the largest energy increase ever seen in any TDE. The off-axis jet scenario also requires the energy to increase with time, with a total energy in the final epoch ∼50 times larger than in the first epoch for $\theta_j = 1/\Gamma$ and ∼5 times larger for $\theta_j = 10°$.

While energy injection has been inferred for TDEs before (e.g., Berger et al. 2012 for Sw J1644+57; but see also Beniamini et al. 2023), the much larger energy increase required for ASASSN-19bt is difficult to explain. The energy in Sw J1644+57 was observed to increase by a factor of ∼20 (Eftekhari et al. 2018), and energy increases were also seen in the nonjetted TDEs AT 2019dsg (factor of ∼10; Cendes et al. 2021a) and AT 2019azh (factor of ∼100; Goodwin et al. 2022). Our nonrelativistic shell model for ASASSN-19bt indicated

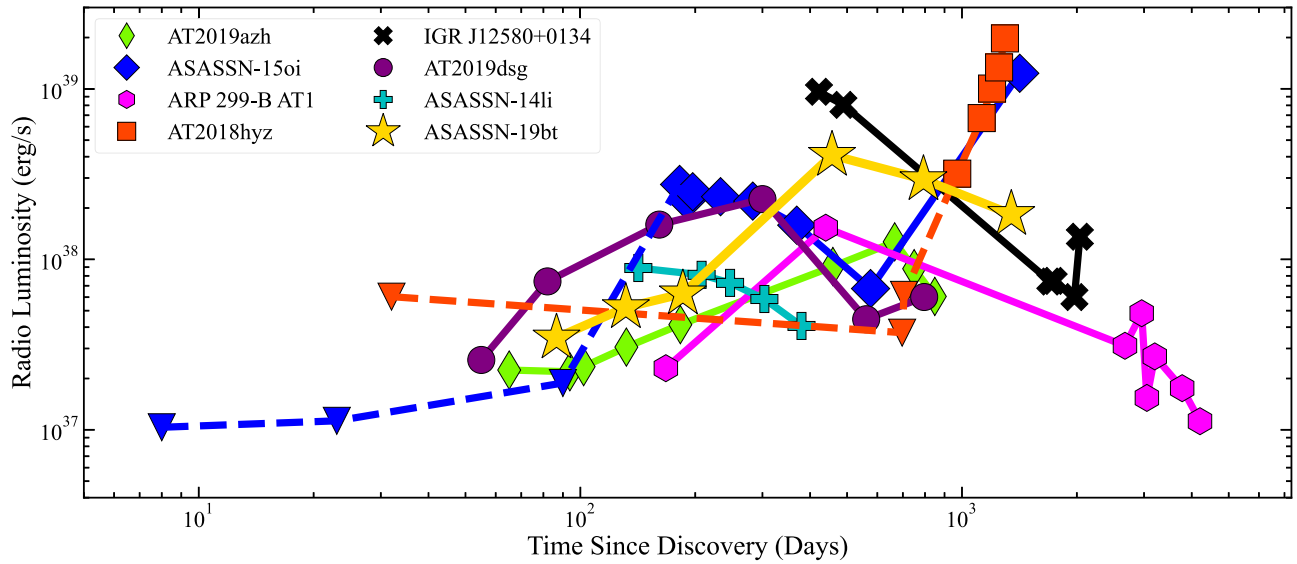

Figure 7. The radio luminosity of ASASSN-19bt at ≈5.5 GHz (*C* band) compared that of other TDEs observed in the radio: ASASSN-14li (Alexander et al. 2016; Goodwin et al. 2022), AT 2018hyz (Cendes et al. 2022), IGR J12580+0134 (Lei et al. 2016; Perlman et al. 2017, 2022), AT 2019dsg (Cendes et al. 2021a, 2024), ASASSN-15oi (Horesh et al. 2021a), ARP 299-B AT1 (Mattila et al. 2018), and CNSS J0019+00 (Anderson et al. 2020).

$E \propto t^{2.2}$ on average, with a steeper dependence during the first four epochs and a shallow dependence for the remaining three epochs. In the off-axis jet model with $\theta_j = 1/\Gamma$, the energy undergoes shallower growth with $E \propto t^{0.1}$ at early times and $E \propto t^{0.7}$ at late times. The energy is declining and then flat for the $\theta_j = 10°$ jet.

While the jet energy we calculate for ASASSN-19bt for the most off-axis viewing angles is similar to that computed for the jetted TDE Sw J1644+57, our model implies a surprisingly large Γ that persists through our last observation at $\delta t \sim 1377$ days (Figure 6, top right panel). This is similar to AT 2018hyz, which was modeled by Matsumoto & Piran (2023) as an off-axis jet. When we repeat their analysis of AT 2018hyz under the same assumptions as we used for ASASSN-19bt, we find that modeling AT 2018hyz as an off-axis jet requires a slightly higher energy, with slightly lower but still relativistic Γ at late times (see Figure 8). In contrast, Sw J1644+57's jet had decelerated to nonrelativistic speeds ($\Gamma \sim 1$) by $\delta t \sim 700$ days (Eftekhari et al. 2018). If the relativistic jet model is correct, it would imply that ASASSN-19bt launched the most highly relativistic outflow seen in any TDE to date. It is difficult to understand how such a jet would remain relativistic to such late times in the high-density nuclear environments in which TDEs occur. The velocity evolution is equally perplexing in the Newtonian model; while the outflow velocities in the non-relativistic model are consistent with those from the sample of optically discovered thermal TDEs, ASASSN-19bt's outflow would have to speed up with time (Figure 6, bottom left panel), which is difficult to understand physically. In steep density profiles, Newtonian shocks can accelerate; however, this requires a much steeper density profile than we infer for ASASSN-19bt (Govreen-Segal et al. 2021).

5.2. Circumnuclear Density

In Figure 9, we show the inferred circumnuclear density profiles for our ASASSN-19bt models compared to those of previously studied TDEs with observed radio emission. To standardize the comparison, we scale the radii by the Schwarzschild radius ($R_s = 2GM_{BH}/c^2$) of the SMBH at the center of each TDE host galaxy and recompute the inferred densities for the thermal TDEs ASASSN-14li, AT 2019dsg, CNSS J0019+00, AT 2018hyz, AT 2020opy, and AT 2020vwl using a standard definition for the volume of the emitting region (a spherical $0.1R$ shell). We use the SMBH masses from K. D. Alexander et al. (2024, in preparation) and references therein (particularly Yao et al. 2024).

The outflow from ASASSN-19bt probes a relatively large fraction of the circumnuclear environment when compared to that of other previously studied TDEs. Both the Newtonian and jet models appear to recover the presence of two separate radial profiles for the magnetic field strength and number density of emitting electrons, corresponding to the pre-brightening and post-brightening portions of the radio light curves. At small r, we find that the density profile under the nonrelativistic model exhibits an $n \propto r^{-3/2}$ slope similar to those of other thermal TDEs such as AT 2020opy and the early epochs of AT 2019dsg (Cendes et al. 2021a; Goodwin et al. 2023b). This is consistent with the classical expectation for spherical Bondi accretion (Bondi 1952). After the blast wave reaches $R \sim 10^{16.5}$ cm, the density increases briefly, then continues to decay at a slightly steeper rate, $n(r) \propto r^{-1.9}$. This is within the range of density profiles previously observed in TDEs, as an $n \propto r^{-2.5}$ profile was inferred for ASASSN-14li (Alexander et al. 2016) and CNSS J0019+00 (Anderson et al. 2020).

In the relativistic model, we estimate the density of the unshocked ambient medium at radius R as $n_{ext} = n_e/4\Gamma^2$, where $n_e = N_e/V$ is the number density of emitting electrons behind the blast wave and $V = \pi R^3/\Gamma^4$ is the volume of the emission region (Barniol Duran et al. 2013). From this, we find that the density profile decays as $n(r) \propto r^{-4.3}$ at early times and as $n(r) \propto r^{-2.6}$ at late times, which is the steepest density profile seen around any TDE to date. We find that ASASSN-19bt exhibits a density profile similar to that of AT 2018hyz if the latter is modeled as an off-axis jet (see Matsumoto & Piran 2023), but our observations span a much wider range of circumnuclear radius.

Along with the steepness of the density profile, the off-axis jet models also yield higher densities at large radii compared to other

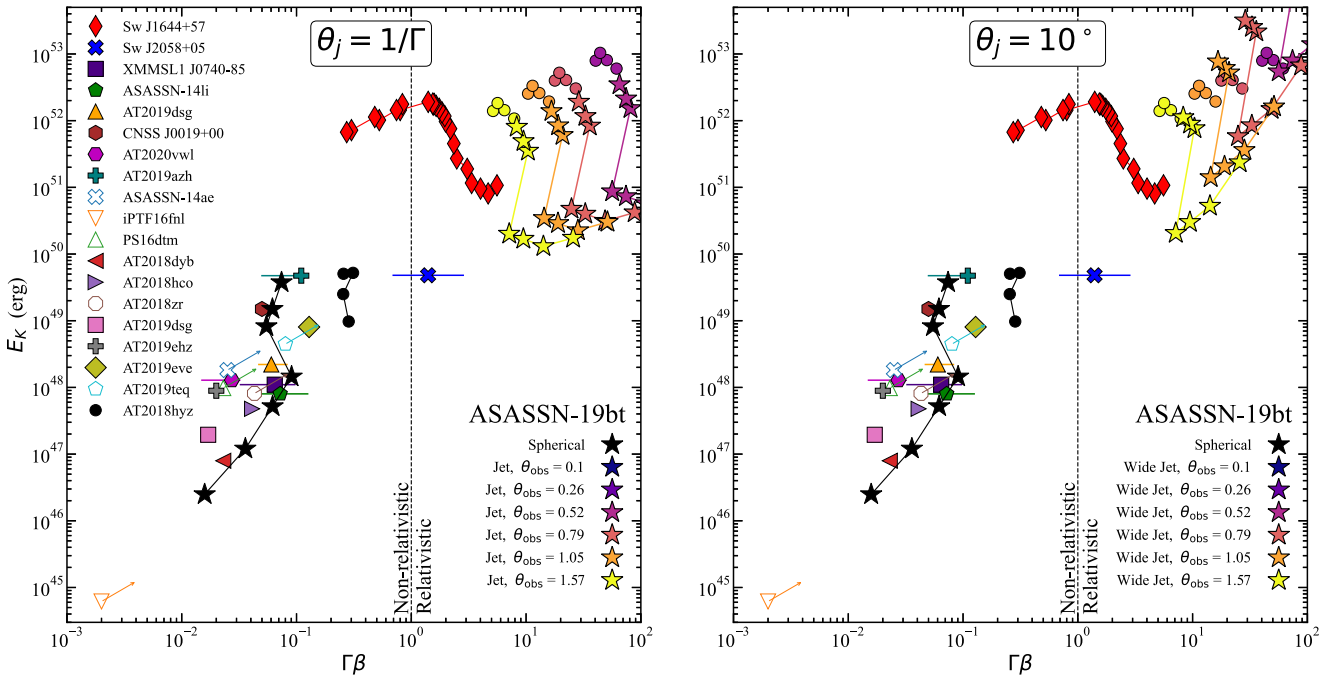

Figure 8. The outflow kinetic energies and velocities inferred from radio emission of known TDEs. The nonrelativistic spherical blast-wave model is represented in black, while the off-axis relativistic jet model is color-coded from indigo to yellow depending on the viewing angle (ASASSN-19bt is denoted by stars, and AT 2018hyz is denoted by circles). We show the relativistic model for a jet opening angle of $\theta_j = 1/\Gamma$ (left) and a fixed opening angle of $\theta_j = 10^\circ$ (right). The data shown for AT 2018hyz are from Cendes et al. (2022) and Matsumoto & Piran (2023). The remaining data are from Sw J1644+57 (Zauderer et al. 2011; Eftekhari et al. 2018; Cendes et al. 2021b), AT 2019dsg (Cendes et al. 2021a, 2023), ASASSN-14li (Alexander et al. 2016), AT 2020vwl (Goodwin et al. 2023a), AT 2019azh (Goodwin et al. 2022), CNSS J0019+00 (Anderson et al. 2020), and Sw J2058+05 (Cenko et al. 2012); all other data are from Cendes et al. (2024).

TDEs (for both ASASSN-19bt and AT 2018hyz). Assuming that the emitting electrons were swept up by the jet, we can approximate the swept-up mass as $M_{\rm swept} \sim m_{\rm p} N_e (\theta_{\rm j})^2 (1/\Gamma_{\rm latest})^2 \simeq 3 \times 10^{-3}\, M_\odot$ for the most off-axis case, assuming a fixed opening angle of $\theta_{\rm j} = 10^\circ$. As the jet is still relativistic and has not yet decelerated, this implies that the total kinetic energy responsible for such a jet is $E_{\rm kin} \gtrsim \Gamma M_{\rm swept} c^2 \simeq 10^{53}$ erg (in the more conservative case, where $\theta_{\rm j} = 1/\Gamma_{\rm latest} < 10^\circ$, then the required energy is lower by a factor of $\sim$2). This energy is among the largest ever inferred for any extragalactic transient; however, it is similar to the energy required by several radio models for Swift J1644+57 (Matsumoto & Piran 2023).

We note that the marginal X-ray detection prior to disruption may indicate the presence of a preexisting weak AGN. Consequently, the observed density enhancement could be attributed to outflowing material colliding with different sections of a preexisting dusty torus. Observations of the TDE ARP 299 suggest that the radio-emitting outflow was briefly embedded within the dusty torus of the host AGN (Mattila et al. 2018). However, modeling of ARP 299 indicated that the torus component was approximately 100 times denser than the external medium, which is significantly higher than the density enhancement observed in the environment of ASASSN-19bt. Therefore, we conclude that the density enhancement around ASASSN-19bt is likely due to a less dense structure (e.g., Zhuang et al. 2024) or multiple outflows, rather than a dense AGN torus.

5.3. Multiple Outflows?

The models described in Section 4 both assume that a single impulsive outflow powers the entire observed radio evolution. However, as previously noted, F_p increases dramatically between $\delta t \sim 186$ days and $\delta t \sim 457$ days. This abrupt radio brightening, together with the presence of a clear discontinuity in the outflow parameters between $\delta t \sim 186$ days and $\delta t \sim 457$ days in both models could suggest the presence of two outflows contributing to the radio emission on different timescales. This scenario would make ASASSN-19bt similar to ASASSN-15oi, which showed two distinct emission episodes in its radio light curve (Horesh et al. 2021a). Modeling of ASASSN-15oi's radio emission revealed that the second emission peak likely corresponds to a more energetic outflow launched several hundred days post-disruption (Hajela et al. 2024).

Following Alexander et al. (2016) and Cendes et al. (2024), we examined the evolution of ASASSN-19bt's emission radius to estimate the outflow launch time for the pre- and post-brightening subsets of the data. For the nonrelativistic model outlined in Barniol Duran et al. (2013), if the outflow is assumed to be moving at a constant velocity, then we can apply a linear fit to the radius evolution and extrapolate to $R = 0$. However, applying a linear fit to all of the data implies a launch date of $\delta t \approx 36.7^{+1.3}_{-1.2}$ days, which is possible but unlikely given the initial radio detection at $\delta t = 40$ days. A linear fit to just the early epochs prior to the rebrightening yields a similarly implausible launch date of $\delta t \approx 39.3^{+1.8}_{-1.5}$ days and overall provides a poor fit to the data. If instead we fit the radius evolution in the early epochs with a power law, we find that a much better fit to the data is obtained if the emitting region is expanding as $R \propto t^{2.3}$. This, however, suggests a dramatic acceleration of the outflow during the first 186 days, which is difficult to explain (as noted in Section 5.1). Linearly extrapolating the radius evolution to the later epochs ($\delta t > 1$ yr) separately would imply a launch date of $\delta t \approx 140.3^{+31.1}_{-26.8}$ days, possibly implying that a

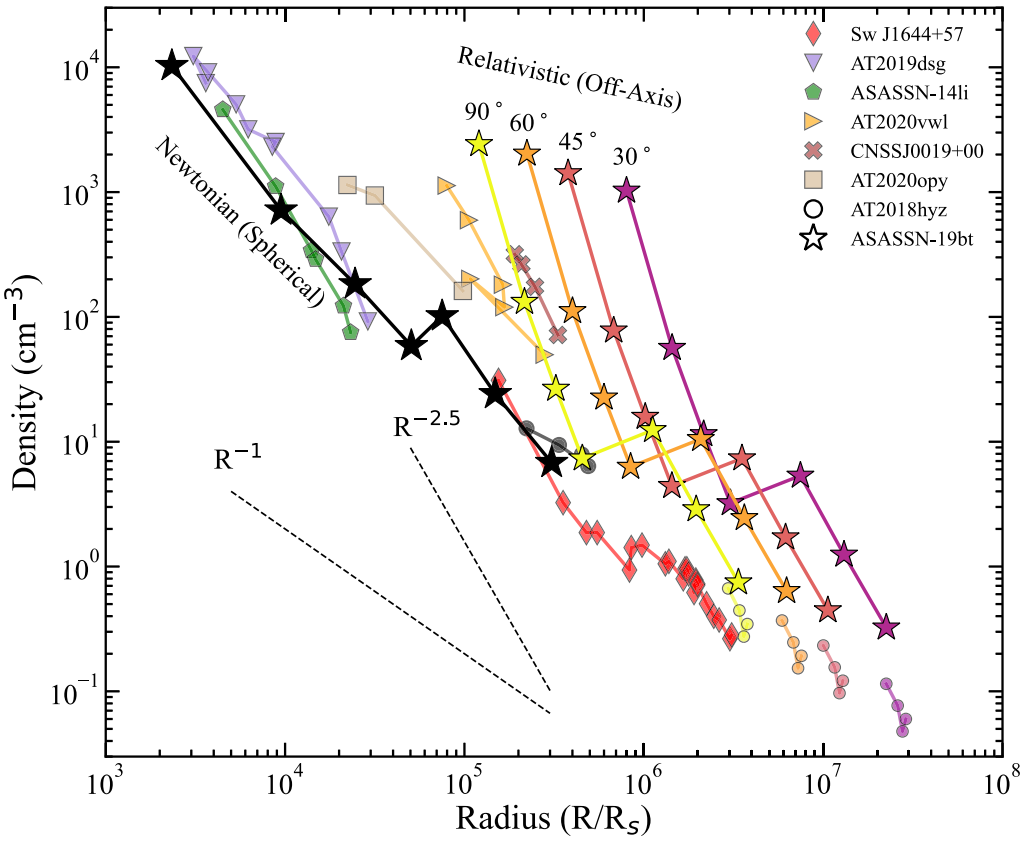

Figure 9. The inferred host galaxy circumnuclear density profile for ASASSN-19bt compared with those of other TDE host galaxies. To standardize the comparison, we give the radii in terms of the Schwarzschild radius ($R_s = 2GM_{\rm BH}/c^2$) of the SMBH at the center of the host galaxy. The nonrelativistic spherical blast-wave model is represented in black, while the off-axis relativistic jet model is color-coded from indigo to yellow depending on the viewing angle. ASASSN-19bt is denoted by stars, and AT 2018hyz is denoted by circles. The AT 2018hyz data are from Cendes et al. (2022) and Matsumoto & Piran (2023). The remaining data and assumed SMBH masses are Sw J1644+57 (Zauderer et al. 2011; Eftekhari et al. 2018; Cendes et al. 2021b), AT 2019dsg (Cendes et al. 2021a), ASASSN-14li (Alexander et al. 2016), AT 2020vwl (Goodwin et al. 2023a), AT 2020opy (Goodwin et al. 2023b), AT 2019azh (Goodwin et al. (2022), and CNSS J0019+00.

second outflow, launched substantially after the time of disruption, powers the latter half of the radio light curve.

For the relativistic solutions outlined in Matsumoto & Piran (2023), a launch date must be assigned in order to solve for the outflow velocity Γ; for our analysis, we set this to be $\delta t = 0$ days. We found that the resulting off-axis jet solutions preferred outflow velocities with $\Gamma \gtrsim 8$. For all viewing angles, Γ decreases by a factor of $\sim$3 over the first 186 days, then increases slightly at 457 days, and then resumes slowly decreasing.

Given the suggested launch date for the later epochs in the nonrelativistic case, we considered the possibility of two relativistic outflows, where one outflow was launched at $\delta t = 0$ days and the other was launched $\sim$140 days later. This still requires $\Gamma \approx 8$ for the emission at $\delta t > 1$ yr in the most off-axis case and does not fully resolve the energy and density discontinuities. Although this is perhaps more physically plausible than the accelerating outflow required in the nonrelativistic case, it is still surprising that even for the most off-axis viewing angles, Γ remains significantly >1 even in our last observation at 1377 days. We further discuss the possible physical mechanisms for powering these various types of outflows in the next section.

5.4. Outflow Mechanism

In order to assess the likelihood of either model, we need to evaluate whether these results are consistent with existing theories describing the origin of radio emission from TDEs. Most TDEs that have received extensive follow-up in the radio are modeled using the Newtonian formalisms outlined in Barniol Duran et al. (2013); therefore, this model for ASASSN-19bt is most easily compared to ones for other TDEs in the literature. The bulk outflow velocity implied by the Newtonian model ($\beta \approx 0.05$) matches well with the expected velocities of $\beta \approx 0.01-0.1$ for winds due to accretion onto an SMBH (e.g., Strubbe & Quataert 2009; Tchekhovskoy et al. 2014). However, outflows launched with these velocities could also be explained by the unbound debris propagating into the circumnuclear medium or ejecta from a collision-induced outflow where the debris fallback stream intersects with itself (e.g., Krolik et al. 2016; Bonnerot & Lu 2020). Nonetheless, these nonrelativistic outflow scenarios all fail to address the apparent acceleration of the outflow in the first 186 days from $\beta \approx 0.016$ to $\beta \approx 0.09$. Moreover, while increasing energy has previously been found to be expected in some nonrelativistic models for TDEs (e.g., Matsumoto et al. 2022), ASASSN-19bt's exceptionally rapid energy increase may be challenging to explain. If the thousandfold increase in the energy is to be attributed to energy injection, it is difficult to conceive of a central engine that remains continuously active for years after the star had been initially disrupted. For example, if we assume that the central engine is only active during the super-Eddington phase, then one would expect the energy injection to stop after approximately 500 days, as that was thought to be the duration

of the super-Eddington phase for Sw J1644+57 based on a rapid shutoff of the X-ray emission at that time (Berger et al. 2012; Mangano et al. 2016). Other on-axis jetted TDEs, such as AT 2022cmc, show even earlier jet shutoff times (Eftekhari et al. 2024). Alternately, energy injection can occur in transients with radially stratified velocities in their ejecta, as previously proposed for some TDEs (e.g., Sw J1644+57; Berger et al. 2012) and other transients (e.g., GW170817; Li et al. 2018). However, the spherical outflow model for ASASSN-19bt requires a larger and more rapid energy increase than either of these cases.

The off-axis relativistic jet scenario avoids the dramatic energy injection required by the nonrelativistic outflow but is also puzzling. We find that the minimal energy of the outflow appears roughly constant at $\sim 2 \times 10^{50}$ erg at early times, then increases to $\sim 7 \times 10^{51}$ erg at late times for the most off-axis cases ($\theta_{\rm obs} \gtrsim 60°$). For a jet with $\theta_{\rm j} = 10°$, the energy decreases by a factor of $\sim$10 during the first 200 days, then remains constant at $E \sim 10^{52}$ erg at later times. It is not clear that this initial energy decrease is physical. Furthermore, as discussed in Section 5.2, a higher total kinetic energy is required such that $M_{\rm jet} > M_{\rm swept}$ to avoid complete deceleration of the jet.

A similar increase in energy was observed in the prototypical jetted TDE Swift J1644+57 on a similar timescale (Eftekhari et al. 2018). In Swift J1644+57, this energy increase may have also been accompanied by a slight density enhancement, similar to (but less dramatic than) the discontinuity in the density profile seen around ASASSN-19bt that accompanies its energy increase (Eftekhari et al. 2018). Berger et al. (2012) argued that the energy injection found in Swift J1644+57 could not be explained by further accretion of the fallback stream and instead is likely due to the relativistic jet launching with a wide range of initial Lorentz factors. However, recently, Beniamini et al. (2023) argued that the observed energy increase can be explained purely by the jet being initially viewed slightly off-axis; as the jet slows down, the beaming cone opens up to reveal more emission. This explanation does not work for ASASSN-19bt, as Γ increases slightly between the two epochs where the energy jumps. Instead, the discrepancy between the early- and late-time energies may indicate the presence of two outflows launched at separate times. A scenario where the accretion rate and subsequent jet launch are significantly delayed relative to peak optical light may explain the presence of a more energetic outflow launched several hundred days post-discovery (e.g., Metzger 2022).

It is also possible that accretion starts earlier and the jet is launched only once the accretion rate falls below some Eddington threshold (Giannios & Metzger 2011; Pasham & van Velzen 2018; Sfaradi et al. 2022). In the case of ASASSN-19bt, the radio rebrightening is not accompanied by a noticeable change in the optical or X-ray emission. However, this hypothesis is difficult to test robustly given the faint X-ray emission (Section 5.5). It is also possible to estimate the accretion rate evolution of TDEs from their optical and UV light curves if certain assumptions are made (e.g., Mockler et al. 2019; Sarin et al. 2024). While a detailed consideration of this point is beyond the scope of this work, we note that even if the accretion disk forms promptly, the accretion rate is likely still too high for ASASSN-19bt's potential second outflow to be launched by a state transition to a highly sub-Eddington ADAF-like accretion flow (Alexander et al. 2024, in preparation).

If the radio emission in ASASSN-19bt is in fact due to a relativistic jet launched away from our line of sight, then one might expect the temporal and energy evolution to follow those of AT 2018hyz. The delayed radio flare in AT 2018hyz may be due to a delayed jet that only breaks out from the spherical disk wind once the the disk/jet system hydrodynamically aligns (Teboul & Metzger 2023). Such a scenario would also naturally give rise to energy injection, which was observed to be by a factor of $\sim$5 (Cendes et al. 2022). A similar phenomenon may be responsible for the delayed flare in ASASSN-19bt's radio light curve and the observed energy injection. In Figures 8 and 9, we show that ASASSN-19bt exhibits radii, energies, outflow velocities, and densities very similar to those of to AT 2018hyz using the off-axis jet model. In contrast, the 5 GHz light curve for ASASSN-19bt appears remarkably different from that of AT 2018hyz (see Figure 7). Furthermore, the radio F_p for ASASSN-19bt is plateauing, which is counterintuitive for an off-axis jet that has not yet decelerated to nonrelativistic speeds. Given the freely expanding jet and steep density profile, this evolution may still be plausible but is not indefinitely sustainable. An important prediction of the off-axis model (if that model is correct) is that Γ should decline in future epochs and the radio luminosity should increase again as the jet decelerates to $\Gamma \sim 1$.

5.5. X-Ray Emission

As seen in Figure 2, TDEs exhibit a range of X-ray luminosities. ASASSN-19bt has the faintest known X-ray emission of any optically selected TDE at $\delta t \lesssim 50$ days and remains faint in the X-rays to late times ($\delta t \sim 700$ days). Initially faint X-ray emission followed by a brightening phase has often been taken as evidence for delayed formation of the accretion disk (e.g., Gezari et al. 2017; Liu et al. 2022). However, Guolo et al. (2024) showed that X-ray obscuration may be a more likely cause. Many models invoke some form of X-ray suppression via the reprocessing of X-ray emission into lower-energy emission by optically thick gas surrounding the black hole. In particular, some have proposed models where the degree of X-ray reprocessing is orientation-dependent (see Dai et al. 2018; Parkinson et al. 2022; Thomsen et al. 2022). In these models, the reprocessing layer is produced by super-Eddington disk outflows, which would result in early-time X-ray suppression corresponding to when the accretion rate was highest. For TDEs with low inclination angles, where the accretion disk is viewed face-on, the expected reprocessing is minimal. However, for high inclination angles, where the disk is viewed nearly edge-on, the reprocessing of X-ray emission is expected to dominate, leading to fainter emission. Under this scenario, one would expect the most X-ray-dim TDEs to be those with the highest inclination angles.

The presence of the cooling break identified in Section 3.1 suggests that the synchrotron emission seen in the radio underpredicts ASASSN-19bt's X-ray emission if extrapolated to X-ray frequencies, requiring an additional emission component. In Swift J1644+57, one model for the X-rays at early times is inverse Compton emission from the jet, which produces a rather hard spectrum (Crumley et al. 2016). For ASASSN-19bt, the measured photon index Γ is significantly harder than the X-rays of most optically selected TDEs (Guolo et al. 2024). Therefore, one possibility is that the X-rays we see in ASASSN-19bt could be inverse Compton emission.

Alternately, the observed X-rays could be intrinsically softer X-ray emission that is highly absorbed. In this case, ASASSN-19bt's exceptionally faint X-ray emission might imply that we are viewing this system nearly perfectly edge-on, which would also be consistent with the most plausible relativistic jet model for the radio emission, where the jet is launched maximally off-axis ($\sim 90^\circ$) with respect to our line of sight. Absorption could also account for the suppression of X-rays unrelated to the TDE; if we consider the marginal pre-disruption X-ray emission as evidence for a preexisting weak AGN, then it is possible that the fainter X-ray emission observed post-TDE is due to stellar debris obscuring the AGN disk. Such a hypothesis was proposed for the TDE PS 16dtm, which was not detected in the X-rays to a limit below an archival X-ray detection of its host galaxy (Blanchard et al. 2017). However, our X-ray spectral modeling found no evidence for intrinsic X-ray absorption, although the limits are not tight. The apparent lack of X-ray absorption by neutral or partially ionized material may be caused by the X-ray-obscuring material in the edge-on disk already being fully ionized.

6. Conclusions

We present the results of our radio and X-ray monitoring of the TDE ASASSN-19bt, spanning nearly 4 yr after the onset of the optical flare. Radio emission was first detected shortly after the optical discovery and continued to rise for years afterward, with the peak radio flux density plateauing $\delta t \gtrsim 1$ yr post-discovery. In contrast, ASASSN-19bt displays very little activity in the X-rays; its early X-ray emission was among the least luminous of any optically selected TDE, and no X-rays have been detected since approximately 225 days post-discovery.

The location of the cooling break suggests that the X-ray emission is not synchrotron emission. We find that ASASSN-19bt's harder X-ray spectrum hints at inverse Compton emission from a possible jet or heavily absorbed softer X-ray emission being viewed through a reprocessing layer (we see no evidence for absorption in the X-ray spectrum, but the constraints are modest due to the faintness of the source). In the latter case, the lack of luminous X-ray emission may be a result of viewing the accretion disk edge-on, as orientation-dependent X-ray reprocessing models predict dim X-rays as seen for ASASSN-19bt.

We employed two models to describe the possible origins of the radio emission: a nonrelativistic spherical blast wave and a relativistic jet launched off-axis from our line of sight. We find that a spherical outflow model would imply a continuous energy rise in the outflow from $\sim 10^{46}$ to $\sim 10^{49}$ erg with speeds in the range $v \approx 0.016c - 0.09c$. A bulk outflow velocity of $\beta \approx 0.05$ agrees with the expected velocities for accretion-driven winds, unbound debris, or collision-induced outflows. Notably, all of these nonrelativistic scenarios fall short in explaining the observed outflow acceleration within the first 186 days. In contrast, the off-axis relativistic model for a jet with $\theta_j = 1/\Gamma$ instead implies that the outflow expands at speeds corresponding to $\Gamma \approx 10$ and has two periods of roughly constant energy at $\sim 2 \times 10^{50}$ to $\sim 7 \times 10^{51}$ erg for the most off-axis cases ($\theta_{obs} \gtrsim 60^\circ$). If we impose a fixed jet opening angle of $\theta_j = 10^\circ$, we instead see decreasing energy at early times and a roughly constant energy of $E \approx 10^{52}$ erg at late times in the maximally off-axis case. The peak flux density and self-absorption frequency both increase ~ 1 yr post-optical peak, implying discontinuities in the magnetic field and density profiles surrounding the SMBH for both models.

We find that the off-axis relativistic jet model alleviates some of the concerns presented by the simple Newtonian model (e.g., the large increase in the energy) but also has some aspects that appear physically implausible (e.g., the overall energy budget). Neither model appears to provide a complete explanation for the radio emission and evolution, suggesting that the true emission geometry is likely more complex than either of the two limiting cases considered here, possibly involving multiple outflow mechanisms operating on different timescales. A key takeaway from this analysis is that more holistic TDE models are needed, incorporating information from emission across the electromagnetic spectrum.

ASASSN-19bt now becomes part of the collection of TDEs demonstrating unusual radio emission in the later stages. Undertaking extended radio observations of these TDEs, particularly at late times ($\sim$years post-disruption), will play a pivotal role in understanding the mechanisms behind the late-time radio emission displayed by a growing number of TDEs. We particularly emphasize the importance of very long baseline interferometry (VLBI) observations for nearby TDEs, as they are crucial for directly testing the off-axis relativistic jet hypothesis. The perpendicular motion of the jet relative to our line of sight makes VLBI observations of centroid motion a definitive smoking gun for relativistic jets within these systems (Mattila et al. 2018). Careful interpretation of the physical parameters derived from the equipartition process may be needed on an event-by-event basis to properly distinguish between truly nonrelativistic outflows and highly off-axis jets, with implications for the overall occurrence rate of powerful jets in TDEs.

Acknowledgments

We thank the anonymous referee for the helpful comments, which improved this manuscript. The Australia Telescope Compact Array is part of the Australia Telescope National Facility (https://ror.org/05qajvd42), which is funded by the Australian Government for operation as a National Facility managed by CSIRO. We acknowledge the Gomeroi people as the traditional owners of the observatory site. The National Radio Astronomy Observatory (NRAO) is a facility of the National Science Foundation operated under cooperative agreement by Associated Universities, Inc. C.T.C. and K.D.A. acknowledge support provided by the NSF through award SOSPA9-007 from the NRAO and award AST-2307668. This work was partially supported by the Australian government through the Australian Research Council's Discovery Projects funding scheme (grant No. DP200102471). The MeerKAT telescope is operated by the South African Radio Astronomy Observatory, which is a facility of the National Research Foundation, an agency of the Department of Science and Innovation. The Berger Time-Domain Group at Harvard is supported by NSF and NASA grants. M.F.B. acknowledges computing and office support from York University, Toronto, Canada. E.R.R. thanks the Heising-Simons Foundation, NSF (AST-2150255 and AST-2307710), Swift (grant Nos. 80NSSC21K1409 and 80NSSC19K1391), and Chandra (22-0142) for support. F.D.C. acknowledges support from the DGAPA/PAPIIT grant No. IN113424.

This paper makes use of the following ALMA data: ADS/JAO.ALMA#2018.1.01766.T. ALMA is a partnership of ESO (representing its member states), NSF (USA) and NINS

(Japan), together with NRC (Canada), NSTC and ASIAA (Taiwan), and KASI (Republic of Korea), in cooperation with the Republic of Chile. The Joint ALMA Observatory is operated by ESO, AUI/NRAO, and NAOJ. We acknowledge the use of public data from the Swift data archive. This paper employs a list of Chandra data sets, obtained by the Chandra X-ray Observatory, contained in doi:10.25574/cdc.260, and is partially based on observations made by the Chandra X-ray Observatory under program DDT-20708675 (ObsIDs 22182 and 22183; PI: Alexander) and software provided by the Chandra X-ray Center (CXC) in the application package CIAO.

Appendix
Total Flux SED Fits and Equipartition Analysis

As described in Section 2.2, we detect archival radio emission from the host galaxy of ASASSN-19bt that predates the TDE. We therefore opted to subtract off a quiescent emission component scaled to this detection and assumed to be constant in time, modeling only the transient emission component. For completeness, here we show the observed SEDs without subtracting any host component, their model fits, and the extracted outflow parameters using the same methods outlined in Section 4 (Figures 10–12 and Table 5). We note that these results do not alter the basic conclusions of our analysis. In particular, at late times, the assumed host galaxy emission component is much fainter than the transient emission component at all frequencies; thus, the parameters at late times are virtually unchanged.

Table 5
Inferred Values for ϵ_B Assuming Different Outflow Geometries

$\theta_{\rm rad}$	$\theta_{\rm deg}$	$\epsilon_{B,\rm transient}$	$\epsilon_{B,\rm total\ flux}$
	Off-axis Relativistic Jet		
0.1	6°	0.0003	0.0016
0.26	15°	0.001	0.004
0.52	30°	0.002	0.008
0.79	45°	0.003	0.012
1.05	60°	0.003	0.016
1.57	90°	0.005	0.022
	Nonrelativistic Spherical Outflow		
…	…	0.2	0.65

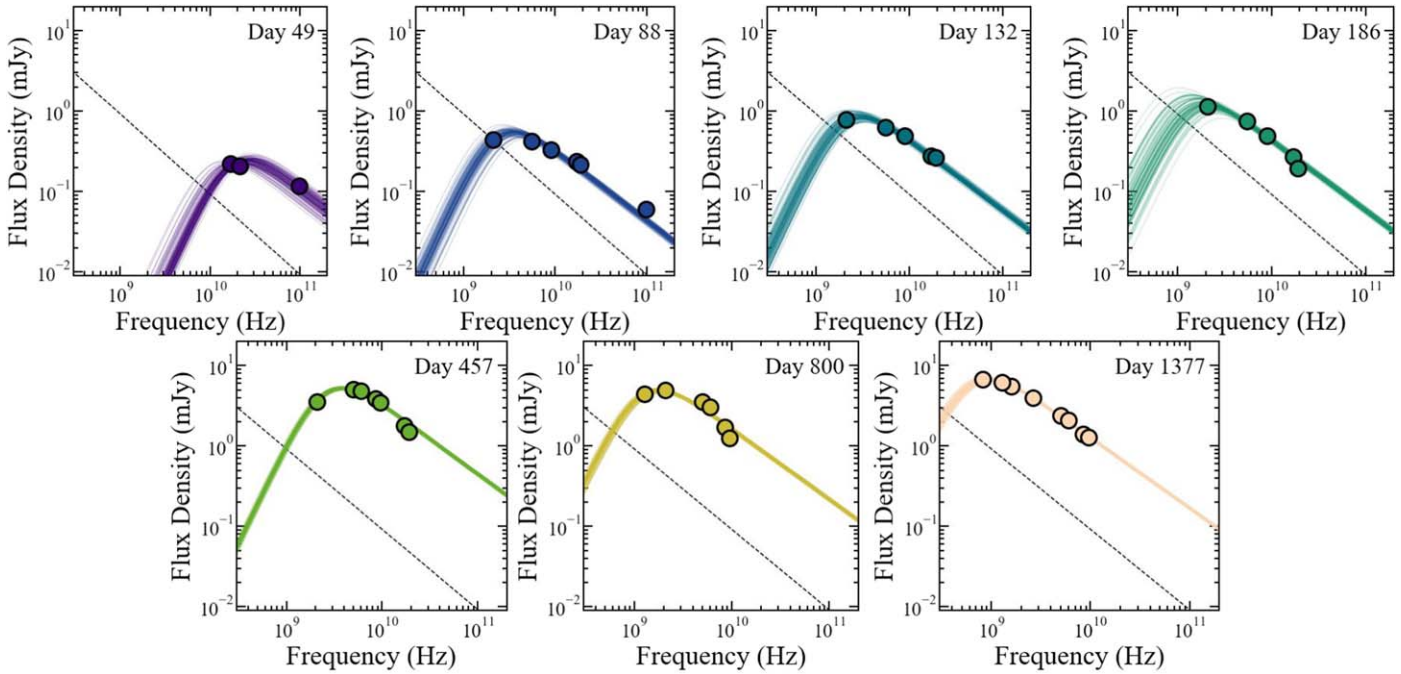

Figure 10. Radio SED fits to the observed ATCA, ALMA, and MeerKAT data assuming no quiescent radio component. The dashed line indicates the assumed quiescent component that we subtracted during our main analysis. The solid lines indicate a representative sample of SED fits from the MCMC modeling.

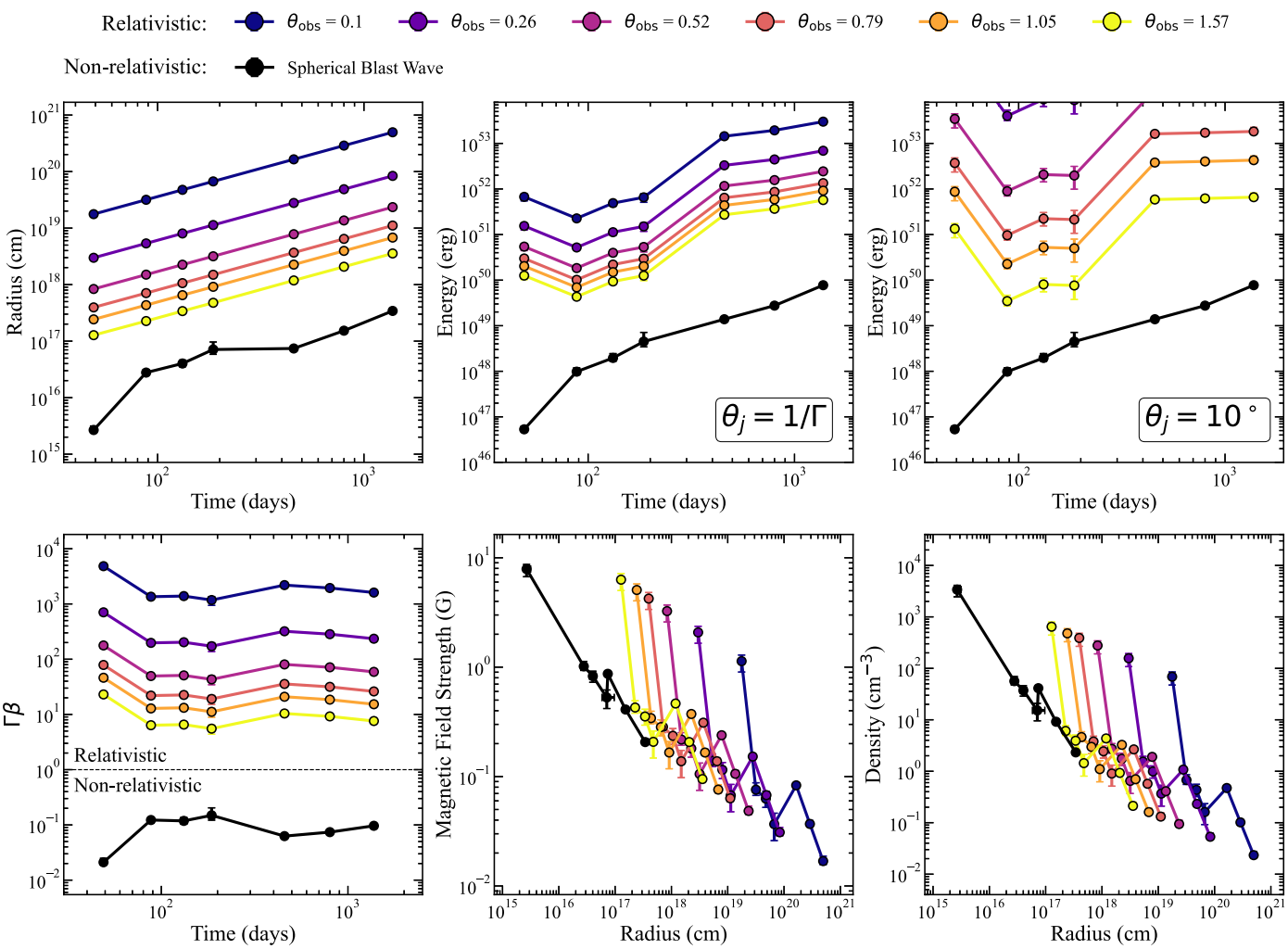

Figure 11. The temporal and radial dependencies of the physical parameters derived from our equipartition calculations assuming no quiescent radio emission. In each panel, we show the results for the nonrelativistic outflow model presented in Barniol Duran et al. (2013; black circles) and the relativistic solution proposed in Matsumoto & Piran (2023; indigo–yellow circles) for a set of off-axis viewing angles. We show the radius of the emitting region as a function of time (top left), the outflow kinetic energy as a function of time for a jet with $\theta_j = 1/\Gamma$ (top middle), the outflow kinetic energy as a function of time assuming a fixed jet opening angle $\theta_j = 10^\circ$ (top right), the velocity evolution of the outflow (bottom left), the radial profile of the magnetic field (bottom middle), and the radial profile of the number density of electrons in the emitting region (bottom right). The error bars on the data correspond to one standard deviation computed using an MCMC approach.

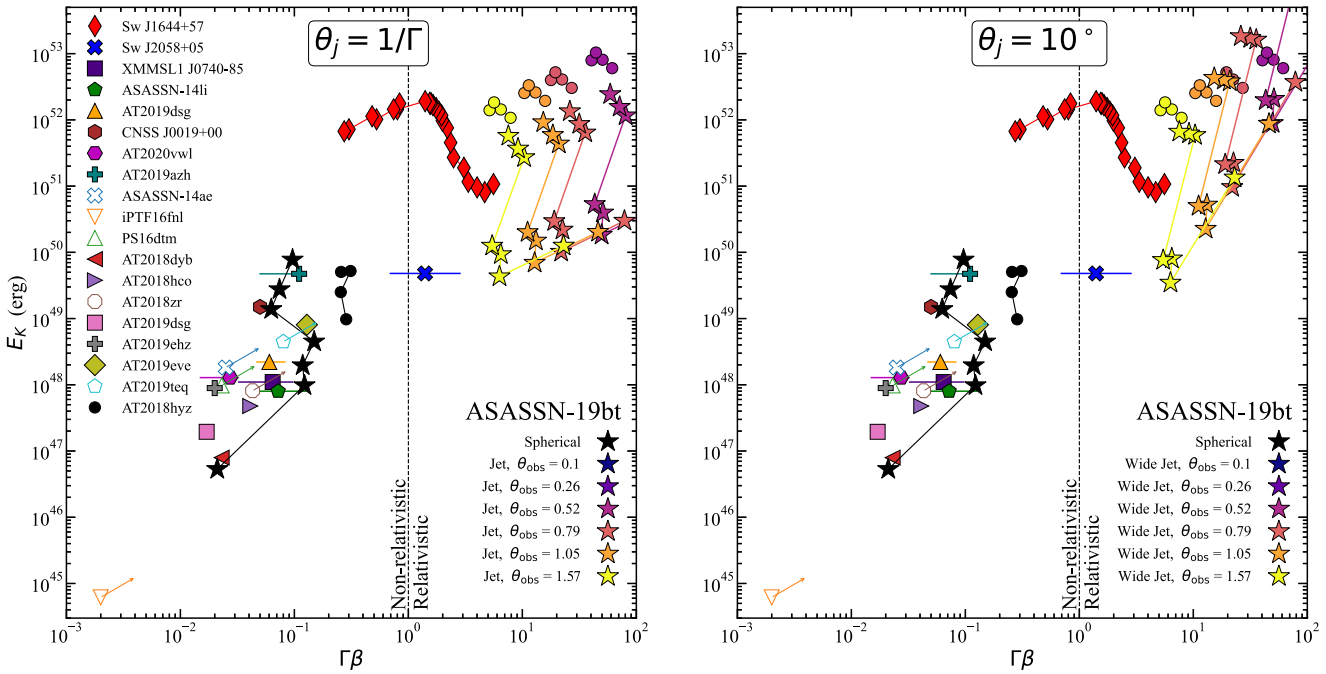

Figure 12. The outflow kinetic energies and velocities inferred from radio emission of known TDEs in context with the inferred energy evolution of ASASSN-19bt from the total flux SED fits. The nonrelativistic spherical blast-wave model is represented in black, while the off-axis relativistic jet model is color-coded from indigo to yellow depending on the viewing angle (ASASSN-19bt is denoted by stars, and AT 2018 is denoted by circles). We show the relativistic model for a jet opening angle of $\theta_j = 1/\Gamma$ (left) and a fixed opening angle of $\theta_j = 10°$ (right). The data shown for AT 2018hyz are from Cendes et al. (2022) and Matsumoto & Piran (2023). The remaining data are from Sw J1644+57 (Zauderer et al. 2011; Eftekhari et al. 2018; Cendes et al. 2021b), AT 2019dsg (Cendes et al. 2021a, 2024), ASASSN-14li (Alexander et al. 2016), AT 2020vwl (Goodwin et al. 2023a), AT 2019azh (Goodwin et al. 2022), CNSS J0019+00 (Anderson et al. 2020), and Sw J2058+05 (Cenko et al. 2012); all other data are from Cendes et al. (2024).

ORCID iDs

Collin T. Christy https://orcid.org/0000-0003-0528-202X
Kate D. Alexander https://orcid.org/0000-0002-8297-2473
Raffaella Margutti https://orcid.org/0000-0003-4768-7586
Mark Wieringa https://orcid.org/0000-0002-7721-8660
Yvette Cendes https://orcid.org/0000-0001-7007-6295
Ryan Chornock https://orcid.org/0000-0002-7706-5668
Tanmoy Laskar https://orcid.org/0000-0003-1792-2338
Edo Berger https://orcid.org/0000-0002-9392-9681
Michael Bietenholz https://orcid.org/0000-0002-0592-4152
Deanne L. Coppejans https://orcid.org/0000-0001-5126-6237
Fabio De Colle https://orcid.org/0000-0002-3137-4633
Tarraneh Eftekhari https://orcid.org/0000-0003-0307-9984
Thomas W.-S. Holoien https://orcid.org/0000-0001-9206-3460
Tatsuya Matsumoto https://orcid.org/0000-0002-9350-6793
James C. A. Miller-Jones https://orcid.org/0000-0003-3124-2814
Enrico Ramirez-Ruiz https://orcid.org/0000-0003-2558-3102
Richard Saxton https://orcid.org/0000-0002-4912-2477
Sjoert van Velzen https://orcid.org/0000-0002-3859-8074

References

Alexander, K. D., Berger, E., Guillochon, J., Zauderer, B. A., & Williams, P. K. G. 2016, ApJL, 819, L25
Alexander, K. D., van Velzen, S., Horesh, A., & Zauderer, B. A. 2020, SSRv, 216, 81
Anderson, M. M., Mooley, K. P., Hallinan, G., et al. 2020, ApJ, 903, 116
Andreoni, I., Coughlin, M. W., Perley, D. A., et al. 2022, Natur, 612, 430
Barniol Duran, R., Nakar, E., & Piran, T. 2013, ApJ, 772, 78
Beniamini, P., Piran, T., & Matsumoto, T. 2023, MNRAS, 524, 1386
Berger, E., Zauderer, A., Pooley, G. G., et al. 2012, ApJ, 748, 36
Blanchard, P. K., Nicholl, M., Berger, E., et al. 2017, ApJ, 843, 106
Bondi, H. 1952, MNRAS, 112, 195
Bonnerot, C., & Lu, W. 2020, MNRAS, 495, 1374
Brown, G. C., Levan, A. J., Stanway, E. R., et al. 2017, MNRAS, 472, 4469
Burrows, D. N., Hill, J. E., Nousek, J. A., et al. 2005, SSRv, 120, 165
CASA Team, Bean, B., Bhatnagar, S., et al. 2022, PASP, 134, 114501
Cendes, Y., Alexander, K. D., Berger, E., et al. 2021a, ApJ, 919, 127
Cendes, Y., Berger, E., Alexander, K. D., et al. 2022, ApJ, 938, 28
Cendes, Y., Berger, E., Alexander, K. D., et al. 2024, ApJ, 971, 185
Cendes, Y., Eftekhari, T., Berger, E., & Polisensky, E. 2021b, ApJ, 908, 125
Cenko, S. B., Krimm, H. A., Horesh, A., et al. 2012, ApJ, 753, 77
Chevalier, R. A. 1998, ApJ, 499, 810
Condon, J. J., Cotton, W. D., & Broderick, J. J. 2002, AJ, 124, 675
Crumley, P., Lu, W., Santana, R., et al. 2016, MNRAS, 460, 396
Dai, L., McKinney, J. C., Roth, N., Ramirez-Ruiz, E., & Miller, M. C. 2018, ApJL, 859, L20
De Colle, F., Guillochon, J., Naiman, J., & Ramirez-Ruiz, E. 2012, ApJ, 760, 103
Duffell, P. C., & Laskar, T. 2018, ApJ, 865, 94
Eftekhari, T., Berger, E., Zauderer, B. A., Margutti, R., & Alexander, K. D. 2018, ApJ, 854, 86
Eftekhari, T., Tchekhovskoy, A., Alexander, K. D., et al. 2024, arXiv:2404.10036
Evans, P. A., Beardmore, A. P., Page, K. L., et al. 2009, MNRAS, 397, 1177
Foreman-Mackey, D., Hogg, D. W., Lang, D., & Goodman, J. 2013, PASP, 125, 306
Gehrels, N., Chincarini, G., Giommi, P., et al. 2004, ApJ, 611, 1005
Gezari, S., Cenko, S. B., & Arcavi, I. 2017, ApJL, 851, L47
Giannios, D., & Metzger, B. D. 2011, MNRAS, 416, 2102
Goldstein, A., Connaughton, V., Briggs, M. S., & Burns, E. 2016, ApJ, 818, 18
Goodwin, A. J., van Velzen, S., Miller-Jones, J. C. A., et al. 2022, MNRAS, 511, 5328
Goodwin, A. J., Alexander, K. D., Miller-Jones, J. C. A., et al. 2023a, MNRAS, 522, 5084
Goodwin, A. J., Miller-Jones, J. C. A., van Velzen, S., et al. 2023b, MNRAS, 518, 847
Govreen-Segal, T., Nakar, E., & Levinson, A. 2021, ApJ, 907, 113

Granot, J., & Sari, R. 2002, ApJ, 568, 820
Guolo, M., Gezari, S., Yao, Y., et al. 2024, ApJ, 966, 160
Hajela, A., Alexander, K. D., Margutti, R., et al. 2024, arXiv:2407.19019
Hills, J. G. 1975, Natur, 254, 295
Holoien, T. W. S., Vallely, P. J., Auchettl, K., et al. 2019, ApJ, 883, 111
Horesh, A., Cenko, S. B., & Arcavi, I. 2021a, NatAs, 5, 491
Horesh, A., Sfaradi, I., Fender, R., et al. 2021b, ApJL, 920, L5
Jiang, Y.-F., Guillochon, J., & Loeb, A. 2016, ApJ, 830, 125
Kalberla, P. M. W., Burton, W. B., Hartmann, D., et al. 2005, A&A, 440, 775
Kochanek, C. S., Shappee, B. J., Stanek, K. Z., et al. 2017, PASP, 129, 104502
Krolik, J., Piran, T., Svirski, G., & Cheng, R. M. 2016, ApJ, 827, 127
Lei, W.-H., Yuan, Q., Zhang, B., & Wang, D. 2016, ApJ, 816, 20
Li, B., Li, L.-B., Huang, Y.-F., et al. 2018, ApJL, 859, L3
Liu, X.-L., Dou, L.-M., Chen, J.-H., & Shen, R.-F. 2022, ApJ, 925, 67
Mangano, V., Burrows, D. N., Sbarufatti, B., & Cannizzo, J. K. 2016, ApJ, 817, 103
Margalit, B., & Quataert, E. 2021, ApJL, 923, L14
Margutti, R., Zaninoni, E., Bernardini, M. G., et al. 2013, MNRAS, 428, 729
Matsumoto, T., & Piran, T. 2023, MNRAS, 522, 4565
Matsumoto, T., Piran, T., & Krolik, J. H. 2022, MNRAS, 511, 5085
Mattila, S., Pérez-Torres, M., Efstathiou, A., et al. 2018, Sci, 361, 482
Metzger, B. D. 2022, ApJL, 937, L12
Metzger, B. D., Giannios, D., & Mimica, P. 2012, MNRAS, 420, 3528
Mockler, B., Guillochon, J., & Ramirez-Ruiz, E. 2019, ApJ, 872, 151
Panaitescu, A., & Kumar, P. 2002, ApJ, 571, 779
Parkinson, E. J., Knigge, C., Matthews, J. H., et al. 2022, MNRAS, 510, 5426
Pasham, D. R., & van Velzen, S. 2018, ApJ, 856, 1
Pasham, D. R., Lucchini, M., Laskar, T., et al. 2023, NatAs, 7, 88
Perlman, E. S., Meyer, E. T., Wang, Q. D., et al. 2017, ApJ, 842, 126
Perlman, E. S., Meyer, E. T., Wang, Q. D., et al. 2022, ApJ, 925, 143
Pushkarev, A. B., Kovalev, Y. Y., Lister, M. L., & Savolainen, T. 2017, MNRAS, 468, 4992
Rees, M. J. 1988, Natur, 333, 523
Riccio, G., Yang, G., Małek, K., et al. 2023, A&A, 678, A164
Ricker, G. R., Winn, J. N., Vanderspek, R., et al. 2015, JATIS, 1, 014003
Rouco Escorial, A., Fong, W., Berger, E., et al. 2023, ApJ, 959, 13
Sari, R., Piran, T., & Narayan, R. 1998, ApJL, 497, L17
Sarin, N., Hübner, M., Omand, C. M. B., et al. 2024, MNRAS, 531, 1203
Sault, R. J., Teuben, P. J., & Wright, M. C. H. 1995, in ASP Conf. Ser. 77, Astronomical Data Analysis Software and Systems IV, ed. R. A. Shaw, H. E. Payne, & J. J. E. Hayes (San Francisco, CA: ASP), 433
Sfaradi, I., Beniamini, P., Horesh, A., et al. 2024, MNRAS, 527, 7672
Sfaradi, I., Horesh, A., Fender, R., et al. 2022, ApJ, 933, 176
Shappee, B. J., Prieto, J. L., Grupe, D., et al. 2014, ApJ, 788, 48
Strubbe, L. E., & Quataert, E. 2009, MNRAS, 400, 2070
Tchekhovskoy, A., Metzger, B. D., Giannios, D., & Kelley, L. Z. 2014, MNRAS, 437, 2744
Teboul, O., & Metzger, B. D. 2023, ApJL, 957, L9
Thomsen, L. L., Kwan, T. M., Dai, L., et al. 2022, ApJL, 937, L28
van Velzen, S., Frail, D. A., Körding, E., & Falcke, H. 2013, A&A, 552, A5
Williams, P. K. G., Allers, K. N., Biller, B. A., & Vos, J. 2019, RNAAS, 3, 110
Yao, Y., Lu, W., Harrison, F., et al. 2024, ApJ, 965, 39
Zauderer, B. A., Berger, E., Soderberg, A. M., et al. 2011, Natur, 476, 425
Zhuang, J., Shen, R.-F., Mou, G., & Lu, W. 2024, arXiv:2406.08012